Super-Resolution Localization and Readout of Individual Solid-State Qubits

by

Eric Bersin

Submitted to the Department of Electrical Engineering and Computer Science
in partial fulfillment of the requirements for the degree of

Masters of Science in Electrical Engineering and Computer Science

at the

MASSACHUSETTS INSTITUTE OF TECHNOLOGY

February 2018

Author .....
Department of Electrical Engineering and Computer Science
February 1, 2018

Certified by .....
Dirk Robert Englund
Associate Professor of Electrical Engineering and Computer Science
Thesis Supervisor

Accepted by .....
Leslie A. Kolodziejski
Professor of Electrical Engineering and Computer Science
Chair, Department Committee on Graduate Theses

Super-Resolution Localization and Readout of Individual Solid-State Qubits

by

Eric Bersin

Submitted to the Department of Electrical Engineering and Computer Science
on February 1, 2018, in partial fulfillment of the
requirements for the degree of
Masters of Science in Electrical Engineering and Computer Science

Abstract

A central goal in quantum information science is to establish entanglement across multiple quantum memories in a manner that allows individual control and readout of each constituent qubit. In the area of solid state quantum optics, a leading system is the negatively charged nitrogen vacancy center in diamond, which allows access to a spin center that can be entangled to multiple nuclear spins. Scaling these systems will require the entanglement of multiple NV centers, together with their nuclear spins, in a manner that allows for individual control and readout. Here we demonstrate a technique that allows us to prepare and measure individual centers within an ensemble, well below the diffraction limit. The technique relies on optical addressing of spin-dependent transitions, and makes use of the built-in inhomogeneous distribution of emitters resulting from strain splitting to measure individual spins in a manner that is non-destructive to the quantum state of other nearby centers. We demonstrate the ability to resolve individual NV centers with subnanometer spatial resolution. Furthermore, we demonstrate crosstalk-free individual readout of spin populations within a diffraction limited spot by performing resonant readout of one NV during a spectroscopic sequence of another. This method opens the door to multi-qubit coupled spin systems in solids, with individual spin manipulation and readout.

Thesis Supervisor: Dirk Robert Englund
Title: Associate Professor of Electrical Engineering and Computer Science

Acknowledgments

First and foremost, I would like to thank my advisor, Professor Dirk Englund. His boundless energy, keen scientific insight, and unwavering support have served as constant inspiration throughout my time at MIT thus far, and I have no doubt will continue to do so. This project in particular began as a small side endeavor, with fairly modest goals; as things progressed and more opportunities came to light, Dirk consistently pushed me to think bigger and to achieve more, challenging me to produce something beyond what either of us had initially envisioned.

Next, I would like to thank my collaborators. My co-author Michael Walsh has been a persistent bedrock over the past two and a half years, both inside and outside the lab. His influence can be seen all throughout this work (just look for the impressive parts), and I cannot fathom what this project and all others in our lab would look like without him. Sara Mouradian has been equally foundational, contributing towards my growth both as a scientist and as a person. Her perseverance whilst surrounded by constant chaos from Michael and me is worthy of sainthood, and her deep knowledge base in all things quantum optics is a well that never seems to run dry. In a similar vein, Dr. Matthew Trusheim has been a remarkable colleague, with a never-ending stream of new ideas and a mental catalog of literature that I'm fully convinced is infinite. Matt's enthusiasm for discovery has energized me even on days when nothing is working, and routinely reminds me why I'm here. Last but not least, I owe the entirety of my free-space optics knowledge to the incomprehensibly patient Dr. Tim Schröder. My first year at MIT was more akin to a random walk than a directed search, and Tim was a driving force in getting me on my feet, often in the face of my own lamentations. Tim taught me what it means to work hard, and for that, I owe him my greatest thanks.

Alongside these core coworkers, there were a number of people in the Quantum Photonics Group to whom I am extremely grateful, for companionship both professional and personal. In particular, I would like to thank Hyowon Moon for being the best office buddy I could hope for, Noel Wan for secretly knowing everything about atomic physics, Hyeongrak Chuck Choi for not so secretly knowing everything about atomic physics, Christopher Foy for his

contributions in developing a significant portion of the code used in this work as well as for providing an outlet to discuss the various merits of fictional entities, and Jordan Goldstein, Catherine Lee, Mihika Prabhu, Cheng Peng, Darius Bunandar, Ben Lienhard, and Jacques Carolan for ever-stimulating conversation and company.

In addition to the support given by those named above, this work was supported by a NASA Space Technology Research Fellowship. I am deeply indebted to NASA and the NSTRF team, both for financial aid and for bringing me into a community of scientists and engineers whose brilliance and passion inspire me every time I'm fortunate enough to work with them. I would further like to acknowledge the administrative support staff at MIT who keep our lab running, namely Janice Balzer and David Barnett. Without either of these inimitable individuals, I have no doubt that our lab would cease operations within a matter of weeks.

Finally, I would like to thank my mother Sandi, my father Alex, my sister Elizabeth, and my brother Nicholas, as well as my girlfriend Kori. They have given me unconditional support in everything I do, no matter how far away they may be, and no matter how incomprehensible my babble may become. Their love and encouragement made me the person I am today, and will continue to shape who I am in the years to come.

Contents

List of Figures

Chapter 1

Introduction

Over the past few decades, the introduction of technologies based on the principles of quantum mechanics has had tremendous impact, both economically and in capturing the minds of the public. In particular, concepts from quantum information science have gained significant traction for their promises of faster computations and secure communications, to name a few applications [1]. At present, while there have been a number of remarkable achievements in the field, ranging from prototype quantum repeaters demonstrating loophole-free violations of Bell's inequality [2–4] to small quantum computers with error-correction-extended lifetimes [5], the scale of the systems built remains small, limited to a handful of qubits. Larger systems have been proposed and preliminary devices built, but major challenges remain, including error and crosstalk suppression [6, 7]. Furthermore, the physical size of the resources required to operate these systems is daunting, with even optimistic estimates requiring football field-sized computers [8] in order to gain advantages over classical computers, so-called "quantum supremacy." As such, it is increasingly relevant to consider how these technologies might better scale and to develop new techniques for building larger coupled quantum systems. In this thesis, we explore a technique for performing low-crosstalk readout of individual solid-state defect centers below the diffraction limit that may provide a path forward towards scaling to larger, denser systems of interacting qubits. In particular, we use the negatively charged nitrogen vacancy center in diamond as a platform to test the viability of this scheme, demonstrating 1) super-resolution localization and 2) simultaneous control and serial readout.

1.1 The Nitrogen-Vacancy Center in Diamond

1.1.1 Structure and properties

In the area of solid state quantum optics, the negatively charged nitrogen vacancy center in diamond [9–13] (henceforth referred to simply as the "NV" or "NV center") has emerged as a leading platform for quantum information applications [14]. As shown in Figure 1-1a, it consists of a substitutional nitrogen atom and an adjacent vacancy. Electronically, the NV is a spin-1 system with a triplet ground state that exhibits a number of useful properties for quantum information applications. An external DC magnetic field applied along the NV axis lifts the degeneracy in the spin states and provides access to three distinct, long-lived levels. Since the NV's symmetry gives it an absolute orientation relative to the diamond lattice, there are four possible axial directions, meaning the spin-level splittings (and thus transition frequencies) can be controlled independently for NVs of differing orientations. Transitions can be driven between these levels via microwave (MW) radiation around 2.88 GHz (external magnetic field dependent), allowing coherent control of the spin population. In addition to exhibiting long decay lifetimes, these spin levels exhibit remarkably long phase coherence times approaching seconds at cryogenic temperatures [15].

The NV excited state dynamics also present a number of favorable qualities. Ground-excited transitions around a 637 nm zero-phonon line (ZPL) are largely spin-conserving, enabling optical readout of the spin state. This is aided by the existence of a metastable singlet state that couples exclusively to $|m_s = 1\rangle$ levels in the excited state manifold, and to the $|m_s = 0\rangle$ level in the ground state manifold. The effects of this are two-fold; first, $|m_s = 1\rangle$ population undergoing optical cycling transitions can be "trapped" in the this sideband, leading to spin-dependent fluorescence as NVs in the $|m_s = 1\rangle$ state will be on average darker than those in the $|m_s = 0\rangle$ state. A common technique for measuring the NV spin state is thus to apply above-band excitation at 532 nm and monitor the NV output fluorescence. Second, the ground state coupling of this sideband means that the NV spin state can be initialized with high fidelity simply by exciting the system off-resonantly; population of $|m_s = 0\rangle$ character will cycle between ground and excited levels, while population of $|m_s = 1\rangle$ character will eventually fall through the metastable state into the ground $|m_s = 0\rangle$ levels.

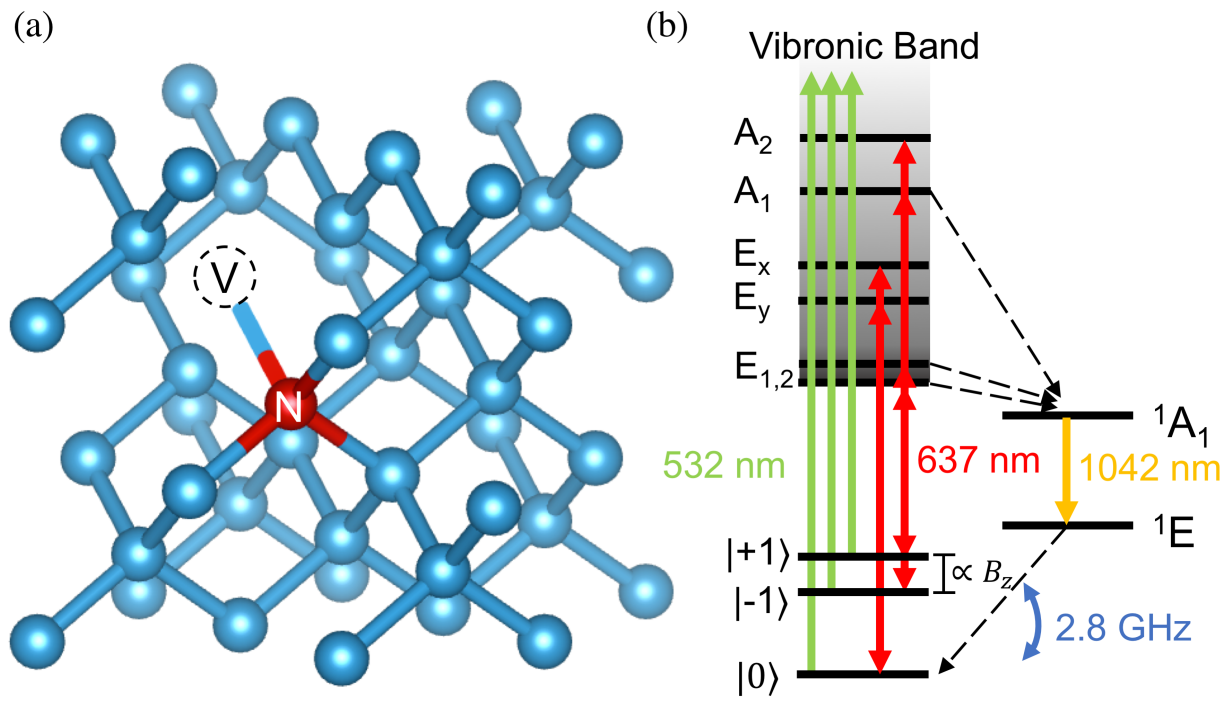

Figure 1-1: (a) The physical structure of the NV center, formed by a substitutional nitrogen atom adjacent to a lattice vacancy. (b) The electronic structure of the NV center, with radiative (solid) and non-radiative (dashed) transitions. Ground state spin levels can be excited via off-resonant 532 nm excitation or resonant excitation near 637 nm. Upon decay, $|m_s = \pm 1\rangle$ excited state levels can couple non-radiatively to a metastable singlet state, which can then undergo further decay to the $|m_s = 0\rangle$ ground state.

These properties are summarized in Figure 1-1b.

Hyperfine interactions between the electronic spin and nearby nuclear spins (either from the always-present nitrogen atom or other nearby carbon-13 nuclei in the lattice) further extend the NV's capabilities as a quantum memory. These nuclear spins generally have an even longer coherence time compared to the electronic spin due to decreased interaction strength with the environment. As a result, single nuclear spin interactions have been used to great effect, for example extending the overall qubit lifetime [16] and performing unconditional quantum teleportation [17], while coupling with multiple nuclear spins has enabled demonstrations of quantum error correction [18].

1.1.2 Scaling quantum algorithms

Unfortunately, this approach of coupling to more and more nuclear spins cannot be scaled indefinitely. Controlling the state of each nuclear spin requires each to have a distinct coupling frequency to the NV electron spin. Since these coupling frequencies are defined by the physical parameters of the system (distance between NV and nuclear spin, NV orientation, etc.), they are uncontrollable, and thus likely to overlap for larger numbers of spins. This approach would also limit the effective logical gate rate; since the NV electron spin is the point of access for the nuclear spins, having one NV limits protocols to interfacing with one physical qubit at a time.

An alternative approach would be to use a hybrid system consisting of multiple coupled NV-nuclear spin systems, with full connectivity given by spin-spin coupling between adjacent NV centers. This coupling has been used to demonstrate entanglement between two NV centers located 25 nm apart [19]. If each NV were to in turn interact with a small (2-4) number of local nuclear spins, this would already provide access to a relatively large subspace for performing quantum algorithms. This approach also cannot scale indefinitely; however, this modest improvement would push the system over an important size threshold - namely, that required for fault-tolerant quantum computing. The error-corrected code mentioned above uses 3 data qubits via the circuit shown in Figure 1-2a, and is not protected against arbitrary qubit errors. Correction of arbitrary errors requires more qubits - for example, the Shor-Bacon code shown in Figure 1-2b requires at least 9 [20, 21]. While systems of many nuclear spins coupled to a single electron spin have been probed [22], scalably realizing such systems with individual control of at least 9 nuclear spins seems an almost unimaginable engineering feat. An alternative approach could be a system of 3 coupled NV centers, each coupled to 3 nearby nuclear spins (one nitrogen and two carbon). The creation of such multi-NV clusters could open the door to a much broader class of quantum algorithms than currently accessible.

One interesting class of algorithms somewhat unique to NV centers includes quantum sensing sequences like NMR. The NV's atomic size and high sensitivity have made it a leading platform for nanoscale sensing applications such as single-molecule magnetic imaging [24].

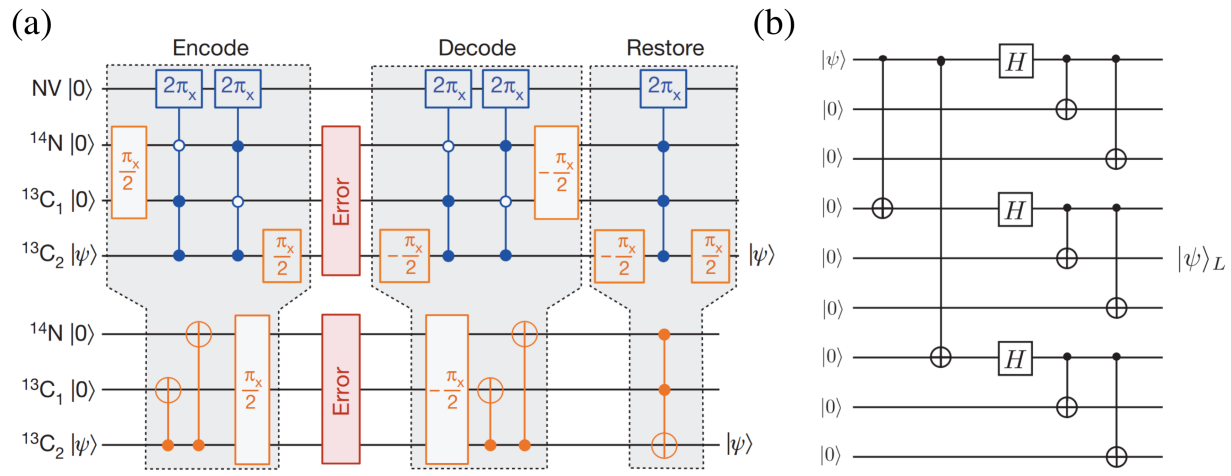

Figure 1-2: (a) Error correcting code used by Waldherr et al. for correcting phase flip errors, taken from [18]. The bottom part shows the code in terms of effective gates on the nuclear spins, while the top part shows the code as implemented via interactions with the NV electronic spin. (b) The circuit required to encode a single qubit with Shor's 9-qubit code for correcting arbitrary single errors, taken from [23]. Note that this is just the encoding, and the decoding and restoring stages are not shown here.

A system of multiple nearby NV centers each sensing the same target could further improve the spatial precision of these techniques. For example, a cluster of NVs could perform simultaneous NMR measurements on a target molecule, then be individually read out to provide triangulated spectroscopic information. If performed on a cluster of spin-spin coupled NVs, it could further enable entanglement-enhanced sensing protocols that beat the standard quantum limit [25, 26].

1.2 Super-resolution readout

All of the above proposals will require NVs that are spatially co-located well below the diffraction limit, such the spin couplings are strong enough to allow for efficient interactions. This poses a problem for the optical readout technique mentioned above, as any readout of one NV will necessarily read the other NVs in the cluster as well. In particular, an error corrected code on such a system would demand low-crosstalk, individual readout to permit the syndrome measurements necessary for error correction. Super-resolution readout is thus

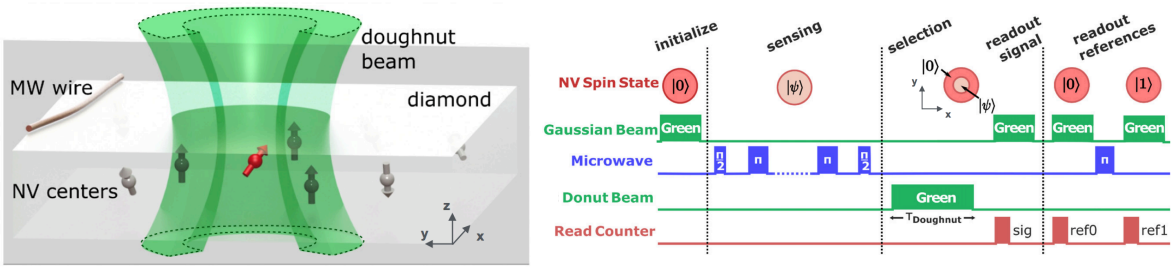

Figure 1-3: Concept image and pulse sequence for a STED-type super-resolution technique known as "spin-RESOLFT," adapted from [27]. After a typical sensing sequence, selective readout is performed by first re-initializing NVs in the area surrounding the target defect using a doughnut-shaped beam, then reading out the entire spot with a traditional Gaussian beam. The data is then retrieved by subtracting this measurement from subsequent reference measurements.

critical in moving forward with such a system. It should be noted that super-resolution spin state control can be achieved without too much difficulty by using NVs of differing lattice orientations and then applying an external magnetic field preferentially aligned to have non-degenerate projections onto each axis orientation. In this way, the spin levels of each NV orientation will be split by a different amount, resulting in unique microwave transition frequencies that can be individually driven.

1.2.1 Existing techniques

In the relatively mature field of quantum sensing, the community has already developed a number of techniques for reading out single NVs below the diffraction limit. One popular class of techniques is based on so-called Stimulated Emission Depletion (STED) Microscopy [27–29], one example of which is shown in Figure 1-3. After performing an algorithm of interest on a spot with one or more NV centers, a beam with a toroidal shape is applied to "deplete" the area surrounding the laser focus. Generally this is a 532 nm source that resets the charge and spin states of NVs in this region. However, the shape of the beam leaves centers in the nanometer-scale focus unexcited, their states still reflecting that of the algorithm's end result. As a result, a subsequent pulse of traditional Gaussian-shaped excitation will induce state-dependent fluorescence from the central region and state-*independent* fluorescence from the reset regions. Subtracting this from a reference measurement (with all NVs reset) yields

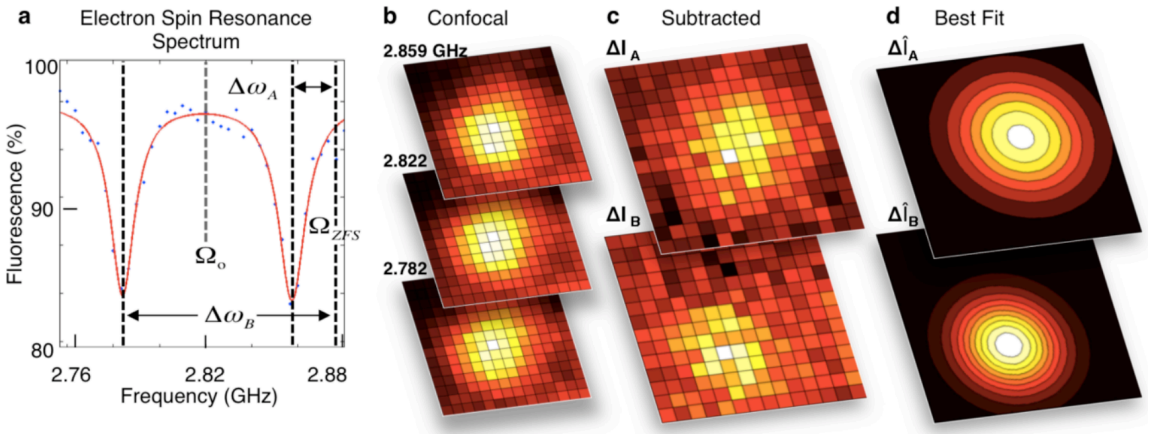

Figure 1-4: Protocol for the DESM super-resolution technique, taken from [32]. NVs with differing orientations and thus distinct MW spin transitions can be modulated independently. Taking fluorescence images at different MW frequencies and subtracting these from reference images thus enables reconstruction of the signals from individual NVs.

a super-resolution measurement of the NV spin states. Other variants on this technique may use orange light (>575 nm) for the final readout to perform charge state-dependent readout[1], but the overall premise is largely the same.

Another recent technique known as Deterministic Emitter Switch Microscopy (DESM) makes use of the aforementioned ability to perform super-resolution control of NV spin states based on their axial orientation with respect to an external magnetic field [32]. As depicted in Figure 1-4, a microwave signal resonant with only one NV orientation selectively modulates the spin state (and thus fluorescence) of that spin. Similarly to the STED techniques, a subsequent measurement using a standard Gaussian beam will measure this modulated fluorescence and unmodulated fluorescence from the surrounding spins, at which point subtracting this sum result from a reference measurement allows extraction of the state of a single desired NV center.

While these techniques allow super-resolution readout of individual NV centers, they are also destructive to the state of nearby centers; that is, in reading out the desired NV, one must reset the states of the surrounding qubits. This makes them unattractive for applications like quantum error correction, where syndrome qubits must be read out in a way that allows for subsequent gates on an unread data qubit, or multi-qubit sensing schemes, where an

[1]Not discussed in detail here, the NV center can also exist in an uncharged spin-1/2 state; this system has a ground-excited transition around 575 nm, and is thus only excited by wavelengths ≤575 nm [30, 31].

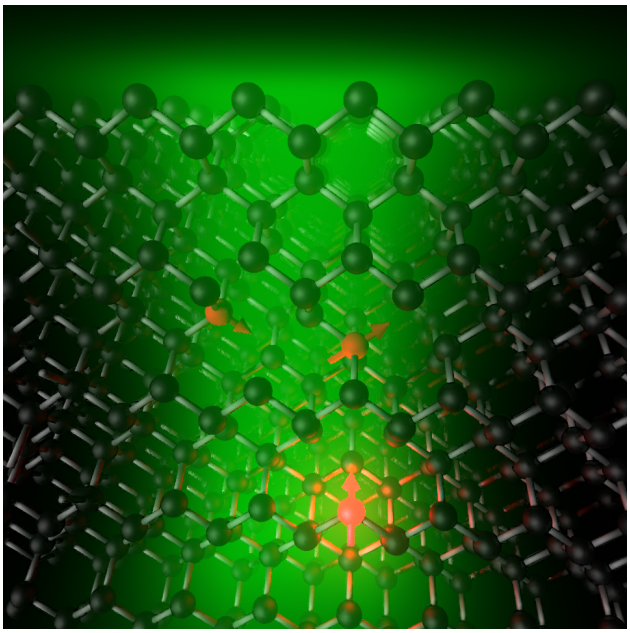

Figure 1-5: Concept image of our technique for individual readout. A laser incident on multiple NVs interacts with only one, inducing fluorescence and allowing state readout, while other nearby defects are left untouched. This figure shows a green laser for clarity; in our implementation, the laser is resonant with the unique transition frequencies of the individual NV being measured, making it red.

advantage would manifest in the ability to read all sensors in a single pulse sequence.

1.2.2 Resonant technique for individual readout

An ideal readout technique would be something like that depicted in Figure 1-5, where a diffraction-limited laser spot, despite illuminating multiple NV centers, is able to induce fluorescence from and read out the state of a single qubit, leaving the others dark and unperturbed. In this thesis, we present a readout technique that realizes this concept. In particular, it circumvents existing issues with current super-resolution techniques by using resonant excitation instead of the traditional above-band excitation. This approach makes use of a feature unique to solid-state qubits: the built-in inhomogeneous distribution of emitters resulting from lattice strain. Since the optical transitions in this system are narrow relative to the distribution of emitter resonances, this allows measurement of individual spins in a manner that protects the quantum states of other nearby centers, with minimal bit-flip or phase errors resulting from readout crosstalk.

1.3 Thesis Outline

Chapter 2 lays out the basic theory behind the operating principle of our technique. We give a brief description of the effects of lattice strain, then provide a derivation of atom-light interactions. Using a simplified two-level model, we compare the fluorescence rate between resonant and detuned NV centers. Finally, we calculate the expected crosstalk for a variety of detunings in the limit of short readout times.

Chapter 3 describes our experiments. We provide details on our optical setup, as well as on the diamond sample preparation and characterization. We then walk through two experiments demonstrating our technique. First, we demonstrate the ability to resolve the locations of multiple NV centers within a diffraction-limited spot. Second, we use this same system to perform simultaneous control and individual readout.

Chapter 4 concludes by looking at the future prospects for our technique. We examine the scalability of the overall principle, and discuss ways to improve and expand upon the existing demonstrations.

Chapter 2

Theory

Our technique is based on two features of atom-like systems in solids. First, the Hamiltonians of these systems contain terms dependent on the local strain of the surrounding lattice, leading to a distribution of resonance frequencies that can often exceed the linewidth of each individual transition. Second, atoms under near-resonant optical illumination will experience population excitation that is strongly dependent on the detuning of the light source from the transition frequency, leading to no excitation in the of case of large detunings and short illumination times. In this chapter, we formally develop the theory for describing these phenomena as applied to the NV center in diamond.

2.1 Strain Dependence of the NV Structure

The Hamiltonian of the NV ^{3}E excited state is given by [13]:

$$H = H_{\text{Coulomb}} + H_{\text{spin-orbit}} + H_{\text{spin-spin}} + H_{\text{strain}} \tag{2.1}$$

The predominant term is the baseline excited state energy given by the Coulomb interaction. The remaining terms lead to the manifold of 6 excited states shown in Figure 1-1. The labels given to these groups describe their character under symmetry operations as determined by group theory analysis [11, 33], and can be used to understand how different interactions affect different levels as depicted in Figure 2-1. The spin-orbit term shifts

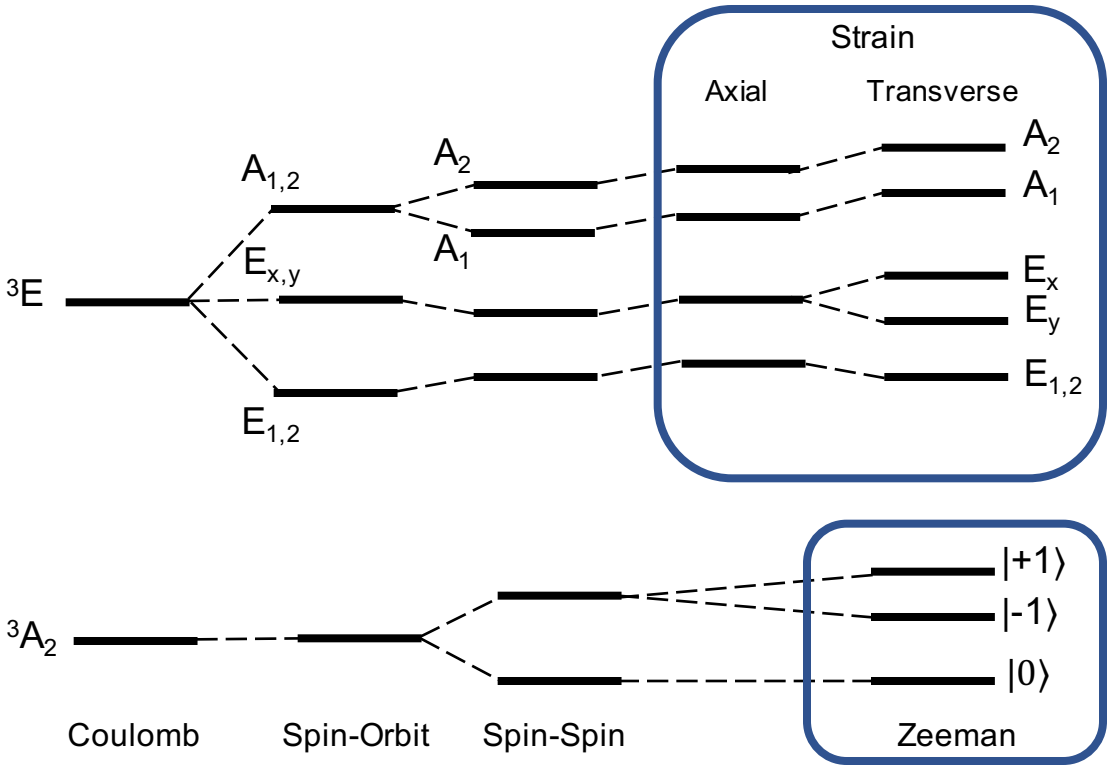

Figure 2-1: The roles of various interactions in splitting out the manifolds of ground and excited state levels.

states based on their total angular momentum, raising the energy of the symmetric A_1 and anti-symmetric A_2 states, lowering the energy of the E_1 and E_2 states, and leaving the zero total angular momentum E_x and E_y states unshifted. The spin-spin interaction lowers the energy of the $E_{x,y}$ states, but raises that of non-zero spin the $E_{1,2}$ states, narrowing the gap between these levels. The $A_{1,2}$ states are split by this interaction. This term also splits out the ground state spin triplet into $|m_s = 0\rangle$ and $|m_s = \pm 1\rangle$ manifolds.

At this point, the lattice strain comes into the picture. As we are primarily concerned with the effect of strain on optical transitions, we here only consider the effect of the strain terms on the excited state levels, which is much stronger than the ~MHz strength effects on the ground states [34] and thus is dominant in determining the transition frequency shifts. The strain Hamiltonian is written [9]:

$$H_{\text{strain}} = \vec{\sigma} \cdot \vec{\hat{V}} \tag{2.2}$$

where $\vec{\sigma}$ is the strain field vector and $\hat{\vec{V}}$ is the vector of orbital operators in the $\{x, y, z\}$ directions. For the NV, the result is that axial strain σ_z shifts all of the excited state levels uniformly. Strain transverse to the NV axis $\sigma_{x,y}$ help to break the symmetry of the center, and lift the degeneracy between the E_x and E_y states. Note that for defect centers with inversion symmetry, while the former interaction would have no effect, the latter would still play a role, making these results pertinent for solid-state emitters beyond the NV.

For completeness, we also note that the Zeeman shift resulting from an axial external magnetic field splits the $|m_s = \pm 1\rangle$ sublevels of the ground state. We include this interaction here as it allows us to drive transitions between singular spin levels, as well as to individually control the spin populations of NVs with differing orientations.

The magnitude of transverse strain splitting is on the order of 1 GHz/MPa [35], with typical samples having strains in the ∼10-100's of MPa range [36]. As we can see, NV centers can be expected to exhibit a wide distribution of transition frequencies that vary by far more than the linewidth of any single center, with a lifetime limit of 13 MHz and a typical broadened linewidth below 1 GHz. Importantly, this is even true for NV centers that are spatially co-located if they have different orientations; though there will be a correlation in strain field for nearby NVs, the differing effects of axial vs. transverse strain mean that these systems could still have significantly different electronic structures.

2.2 Atomic Interactions with Electromagnetic Fields

We now turn our attention to the interactions of NV centers with optical fields, in particular looking at the dynamics under resonant and near-resonant illumination. The transitions between ground and excited states are spin-conserving, cycling transitions; as indicated in Figure 1-1b, the ground $|m_s = 0\rangle$ state couples selectively with the zero-spin excited state E_x and E_y levels, while the ground $|m_s = \pm 1\rangle$ states couple with the net-spin $A_{1,2}$, $E_{1,2}$ levels (which are produced from mixtures of $|m_s = \pm 1\rangle$ states). Furthermore, at cryogenic temperatures, the linewidths of these transitions approach their lifetime limits, around 13 MHz, far smaller than the splitting between excited state levels. It is thus possible to excite the NV in a spin-selective manner using a narrow, resonant laser. This has been used to great success

to produce spin-photon entanglement between the NV and its emission mode [10, 37]; here we explore its usage in selectively reading out an NV based on both its spin state and its strain.

A simplified picture of the NV as a two-level system with a strain dependent resonance shift Δ allows us to build an analytic model for our scheme. In this picture, we can describe the dynamics between the $|m_s = 0\rangle$ ground state (g) and one of the $E_{x,y}$ excited state levels (e) via the typical optical Bloch equations (OBE), which use the density matrix formalism:

$$\dot{\rho_{gg}} = i\Omega\rho_{ge} - i\Omega^*\rho_{eg} + \gamma\rho_{ee} \tag{2.3}$$

$$\dot{\rho_{ee}} = -\dot{\rho_{gg}} \tag{2.4}$$

$$\dot{\rho_{eg}} = i\left(\Delta + \frac{\gamma}{2}\right)\rho_{eg} + i\Omega\left(\rho_{ee} - \rho_{gg}\right) \tag{2.5}$$

$$\dot{\rho_{ge}} = \dot{\rho_{ge}}^* \tag{2.6}$$

where γ is the decay rate of the excited state, and Ω is the Rabi frequency of the NV-laser system.

2.2.1 Steady-state solution

First, we consider the steady-state solutions under continuous illumination for long times $t \gg \gamma^{-1}, \Omega^{-1}$. Setting the above derivatives to zero, we can solve for the excited state population:

$$\rho_{ee} = \frac{2|\Omega|^2}{\gamma^2 + \Delta^2 + 4|\Omega|^2} \tag{2.7}$$

We note that this is an incoherent mixed state, reached after multiple cycles of excitation and decay. As a result, we can calculate the mean fluorescence of this system by simply multiplying the above by the decay rate. It becomes interesting to compare the fluorescence of a strongly detuned $\Delta \gg \gamma$ system with a system on resonance $\Delta = 0$, as might be the case with a pair of NVs experiencing different strain fields. In this scenario, the ratio of their fluorescence rates can be seen to be:

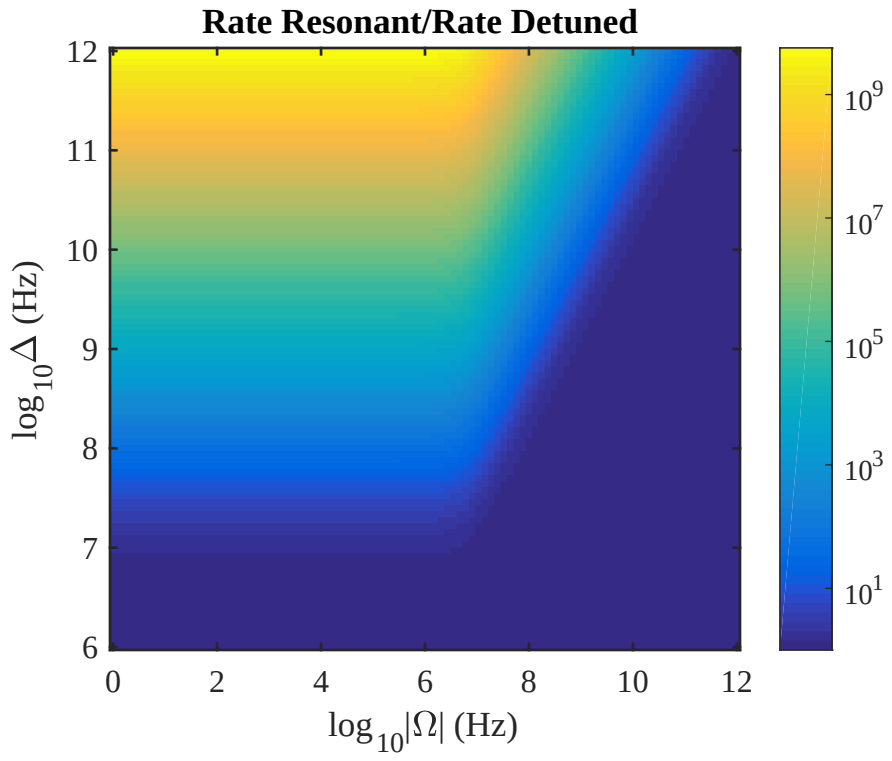

Figure 2-2: Ratio in Eq. 2.8 of steady-state fluorescences from resonant and detuned NVs, for varying detunings and Rabi frequencies with fixed linewidth $\gamma = 13$ MHz.

$$\frac{R_{\text{resonant}}}{R_{\text{detuned}}} = \frac{\Delta^2 + 4|\Omega|^2}{\gamma^2 + 4|\Omega|^2} \tag{2.8}$$

This is plotted for varying detunings and excitation strengths for the case of a lifetime-limited linewidth NV in Figure 2-2. In the most pronounced case — under weak excitation — the fluorescence ratio is a maximum Δ^2/γ^2, allowing significant preferential interaction with one NV over another. For an imaging application, where one desires localization of single NV centers, this can be used to isolate the signals from multiple individual defects, resolving their locations below the diffraction limit, as will be seen in Chapter 3.

2.2.2 Dynamic solution

For the envisioned applications in quantum information, an off-resonant NV may be in a superposition of spin states $\alpha|0\rangle + \beta|1\rangle$ when a nearby NV is being resonantly read out via the narrow laser probe. As seen in the OBE above, the $\alpha|0\rangle$ state population of the

off-resonant NV will experience slight mixing into the excited state, where the population could in turn undergo decay and spontaneously emit. In this case, a single such decay event would be sufficient to collapse the prior spin superposition and destroy the quantum information contained therein. We thus here consider the coherent time evolution dynamics of off-resonant excitation.

There is no general analytical solution to the OBE for arbitrary γ, Ω, Δ. Instead, we can simulate the dynamics using discrete time steps. Doing so for varying detunings yields the results shown in Figure 2-3a. The frequency of the oscillations in population difference are Rabi frequency dependent, with greater detunings oscillating faster. Furthermore, larger detunings are able to drive less population into the excited state compared to the resonant case. However, it is interesting to compare this with the purity of each case, mathematically defined as the trace of the density matrix squared, and intuitively thought of as the degree of coherence of a system. Spontaneous decay is the mechanism by which our two-level system decoheres, and this decay can only happen for population in the excited state. A corollary of detuned systems driving less population into the excited state is that these systems will also undergo experience less decoherence and maintain their purity for longer. As seen in Figure 2-3b, while resonant systems will rapidly decay to highly mixed states [1], detuned systems can maintain a high degree of purity even for long excitation times.

We are interested in using this analysis to find the probability that at least one decay has occurred during the duration of an off-resonant excitation pulse. Since we're interested in the regime where the probability of multiple decays occurring is low, we can consider the dynamics under zero decay. Setting $\gamma = 0$ and solving the OBE, the excited state population undergoes simple Rabi oscillations:

$$\rho_{ee} = \frac{|\Omega|^2}{|\Omega|^2 + \Delta^2} \sin^2\left(t\sqrt{|\Omega|^2 + \Delta^2}\right) \tag{2.9}$$

Since the decay rate will be proportional to the excited state population, this system has an expected number of decay events during a time T:

[1] As density matrices require trace(ρ) = 1, the lowest possible purity (corresponding to the most mixed state) is 0.5.

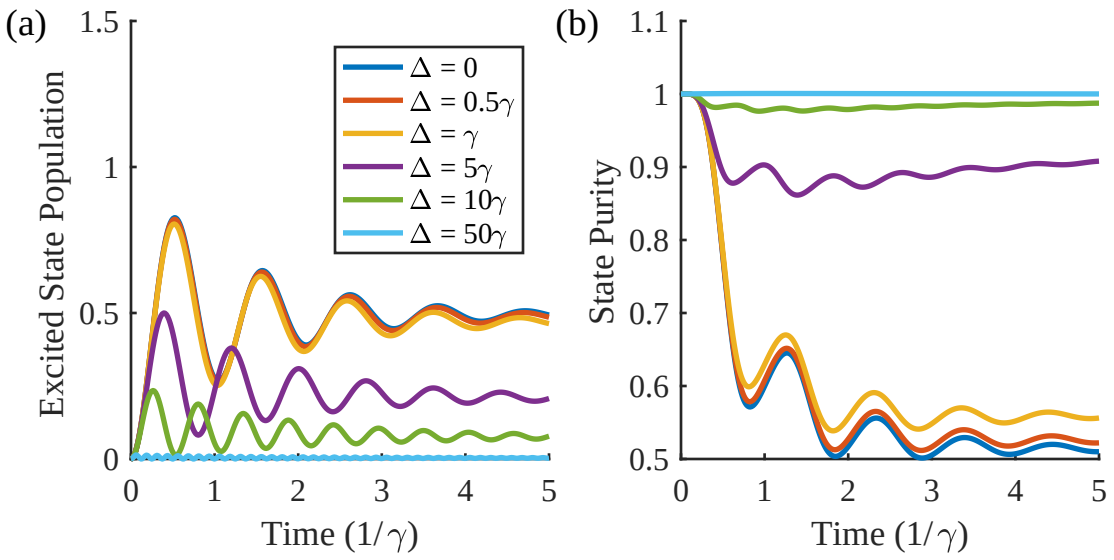

Figure 2-3: (a) The simulated time evolution of a two-level system under optical excitation. The Rabi frequency is fixed at $|\Omega| = 3\gamma$. (b) The corresponding purity of the systems simulated in (a).

$$\begin{aligned}\lambda &= \int_0^T \gamma \rho_{ee} dt \\ &= \frac{\gamma|\Omega|^2}{|\Omega|^2+\Delta^2}\left[\frac{T}{2} - \frac{\sin\left(2T\sqrt{|\Omega|^2+\Delta^2}\right)}{4\sqrt{|\Omega|^2+\Delta^2}}\right] \\ &\approx \frac{\gamma|\Omega|^2 T}{2\left(|\Omega|^2+\Delta^2\right)}\end{aligned} \tag{2.10}$$

where in the last line we take $T \gg \frac{1}{\sqrt{|\Omega|^2+\Delta^2}}$, which is appropriate for any non-pulsed measurement. Following Poissonian statistics, the probability η of no decay events occurring is then:

$$\eta = e^{-\gamma|\Omega|^2 T/2(|\Omega|^2+\Delta^2)} \tag{2.11}$$

To verify this description, we perform a Monte Carlo simulation of the OBE dynamics with no decay. At each time step, the starting state is evolved according to the OBE. After solving for the current state, there is a random number check against the probability $\rho_{ee}\cdot\gamma\cdot dt$ of spontaneous decay; if decay occurs, the current time is recorded and the simulation

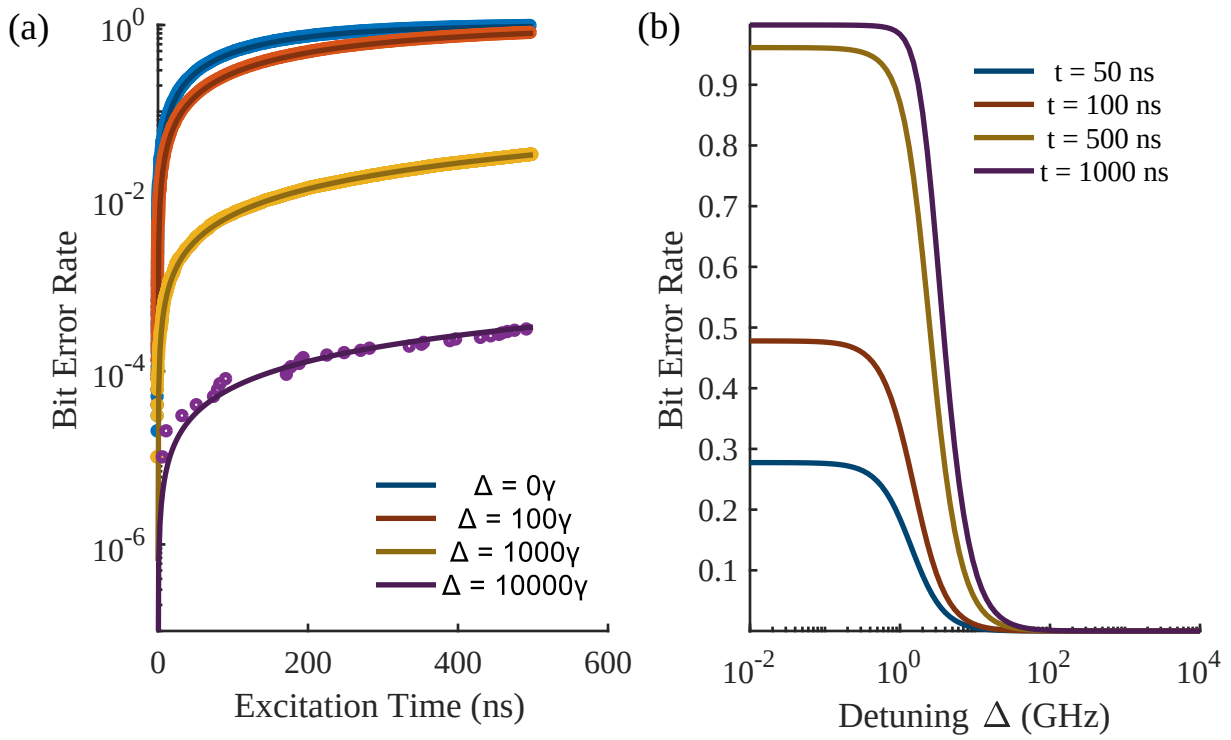

Figure 2-4: (a) The probability of an NV of linewidth $\gamma = 13$ MHz experiencing a decohering spontaneous decay event as a function of time, plotted for varying detunings. This can be understood as a bit error rate in the proposed architecture. Rabi frequency is fixed at $\Omega = 100\gamma$. Circles are from the simulated cumulative density function, and solid lines are from the analytical model, showing good agreement. (b) Bit error rate as a function of detuning, plotted for varying excitation times. Ω and γ are as in (a).

repeated. If no decay occurs, the simulation advances to the next time step. Performing this for 10^5 averages allows us to construct a cumulative density function for the likelihood of decay as a function of excitation time and detuning, presented in Figure 2-4a as a bit-error rate. Another understanding of this same relationship is shown in Figure 2-4b, where we plot the analytical model for bit error rate as a function of detuning for varying total excitation times. As we can see, for excitation times in the 100's of nanoseconds, 10 GHz of detuning is sufficient to suppress the bit error rate to the single percentage range.

2.3 Additional considerations

2.3.1 AC Stark shift phase errors

In addition to bit-flip errors resulting from spontaneous decay, we also consider phase errors resulting from differential AC Stark shift on the $|m_s = 0, 1\rangle$ spin ground states. Following from the OBE, a two-level system under far-detuned excitation experiences an effective energy shift given by $|\Omega|^2/\Delta$, known as the AC Stark shift. As a result of this energy shift, a state will evolve with an additional phase accumulation $\phi = |\Omega|^2 t/\Delta$. In our scheme, both the $m_s = 0$ and $m_s = \pm 1$ levels will shift according to their respective detunings, which may cause one component to pick up phase relative to the other. This becomes a phase error on our qubit, and is given by the difference:

$$\phi = \frac{|E|^2}{\hbar}\left(\frac{\bar{\mu}_0^2}{\Delta_0} - \frac{\bar{\mu}_1^2}{\Delta_1}\right) t \tag{2.12}$$

where $|E$ is the electric field strength, each $\bar{\mu}_i$ is the projection on the field vector of the transition dipole for the spin i ground-excited zero phonon line transition, and each Δ_i is the detuning of the red light from each respective transition. Typically, these transitions will be within $\sim$10 GHz of one another, and the dipole moments roughly equal (though with different projections owing to the different polarizations of the transitions). To get a sense of the order of magnitude, we treat this in the case where $\Delta_1 \gg \Delta_0$, and note that this is a worse scenario than one would typically expect. We then see that the phase error goes simply with:

$$\phi \sim \frac{|\Omega|^2}{\Delta} t \tag{2.13}$$

Taking typical experimental parameters of $|\Omega| \sim \gamma$, $\Delta \sim 100$ GHz, and $t \sim 100$ ns, this phase error is of order 10^{-3}. We further note that under worse conditions, $|\Omega|$, Δ, and t can be well characterized and this phase error corrected. Accordingly, we consider this phase error negligible in moving forward.

2.3.2 Spectral diffusion

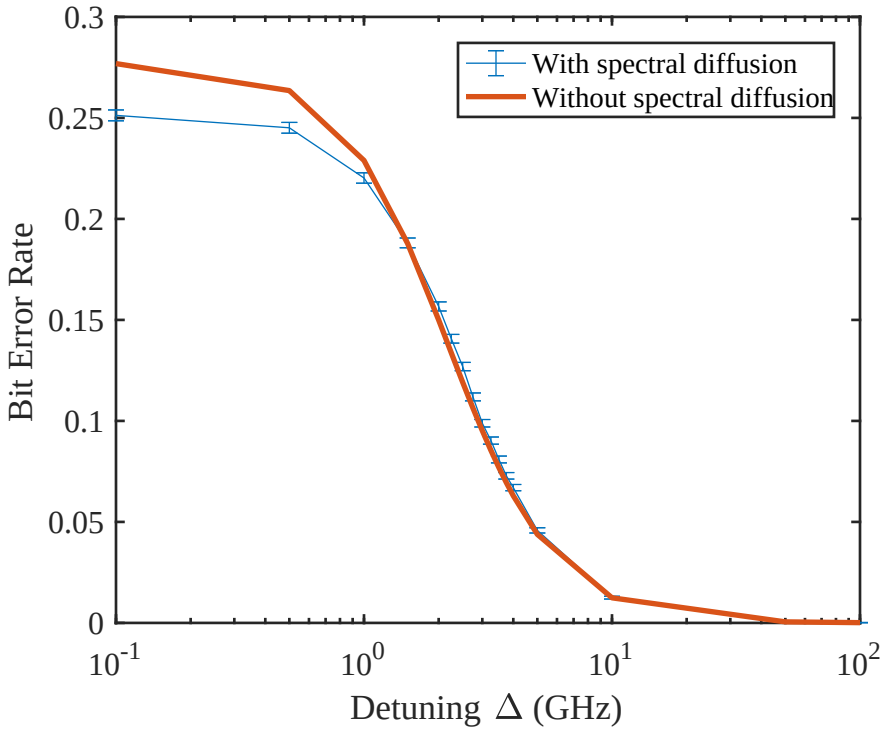

Figure 2-5: Comparison between the bit error rate when assuming a lifetime-limited line versus accounting for spectral diffusion. Parameters fixed at $t_{\text{measure}} = 50$ ns, $\gamma = 13$ MHz, diffusion broadening = 700 MHz (reflecting typical experimental values), and $|\Omega| = 2$ GHz.

While the above theory presumes a static transition frequency, the NV's levels are highly susceptible to external fields, causing large GHz-scale shifts in resonance frequency as its environment fluctuates [38]. This "spectral diffusion" of the ZPL occurs on a microsecond timescale and has been observed to stem from high optical excitation powers [39]. As a result, while the ZPL can be expected to remain relatively single-frequency over the course of a single experiment, from shot-to-shot one expects jumps in the line that lead to an observed broadening over many averages. In our model, this cannot be accounted for by simply using the broadened linewidth, as the emission rate of the system is still that of the lifetime limit. Rather, this effect results in an additional randomized detuning added to the original offset. We account for this in our simulation by incorporating jumps between each average, adding an additional Gaussian-random detuning to each trial, with width given by the observed broadening resulting from this effect. Figure 2-5 shows the results for this modification. As

intuition might suggest, for small detunings, this lowers the net error probability, while at large detunings, the effect is negligible compared to the base starting detuning. Even for the resonant case, the bit error rate is within a few percent of that without spectral diffusion, and so we neglect this effect moving forward.

2.4 Summary

Bringing the picture together, we see that the presence of strain makes it possible to have multiple NV centers with different resonance frequencies within a diffraction limited spot. This is specifically made possible by strain gradients, or by NVs having differing orientations (due to the differing effects of axial and transverse strain). When this splitting is sufficiently strong, it is possible to resonantly read out the state of one NV in a manner that leaves the states of other NVs unaffected with high probabilities. In the following chapter, we present experiments that demonstrate the viability and utility of the theory thus far presented.

Chapter 3

Experimental Results

3.1 Experimental Setup

A scanning confocal cryogenic microscope is used to image samples and to address single NV centers. Cryogenic temperatures are required to freeze out phonons that broaden the excited state levels, letting us resolve the individual ground-excited transitions needed for our technique. The full schematic is depicted in Figure 3-1. Lasers at 532 nm (Coherent Verdi G5) and tunable near 637 nm (New Focus Velocity 6304) pass through individual accousto-optical modulators to allow laser on-off modulation, controlled via TTL pulses (SpinCore PulseBlaster ESR Pro) with 2 ns resolution. A portion of the red laser emissions are split off and fed to a wavemeter (HighFinesse WS7-60), which can both read out the frequency to 10 MHz precision and lock the laser frequency through a PID control loop that feeds back to the laser diode. The green and red emissions are combined in a wavelength multiplexer (Thorlabs RGB26HF) and sent to the main optical setup. After shortpass filtering (Semrock FF01-650) to remove fluorescence noise, a 90:10 beamsplitter sends 10% of the laser towards a confocal setup. Scanning galvanometer mirrors (Nutfield QS-5 OPD) followed by a 4F imaging system incident on a 0.95 NA achromatic objective comprise a scanning confocal microscope, where changes in the galvo angles manifest as planar spatial scanning of the focal spot. This objective sits at room temperature in a cryostat (Montana Instruments), separated from the main 4 Kelvin chamber by a radiation shield. Piezo stages (Attocube) inside the chamber allow nanometer positioning of a sample.

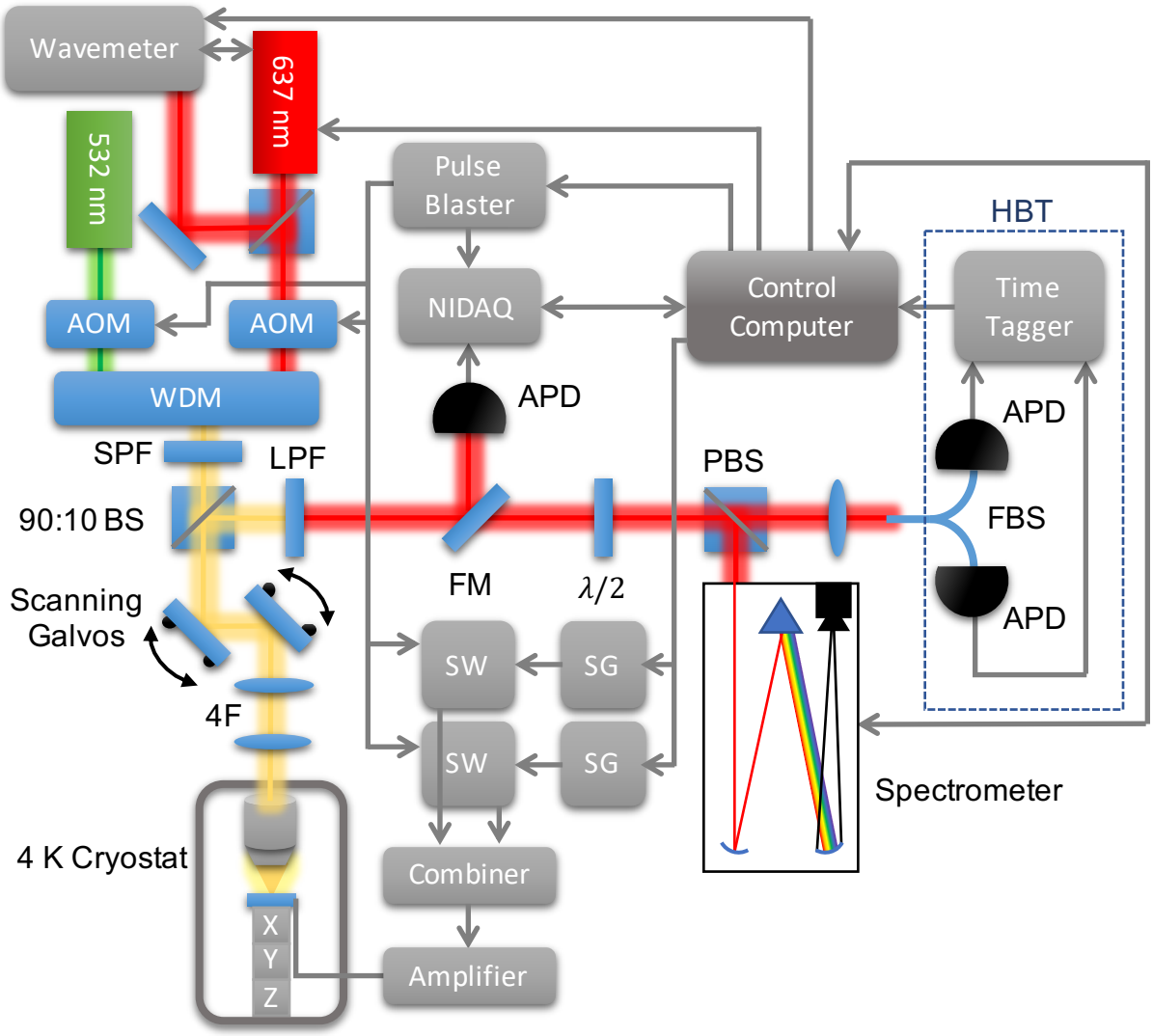

Figure 3-1: Block schematic of the cryogenic confocal microscope used to perform our experiments, with details given in main text. AOM = accousto-optical modulator, WDM = wavelength (de)multiplexer, BS = beamsplitter, PBS = polarizing beamsplitter, SPF = shortpass filter, LPF = longpass filter, SG = MW signal generator, SW = MW switch, FM = flip mirror, $\lambda/2$ = motorized half-wave plate, APD = avalanche photodiode, FBS = fiber beamsplitter, NIDAQ = National Instruments Data Acquisition Device, HBT = Hanbury Brown and Twiss interferometer.

Emissions from the sample trace back the excitation path up to the beamsplitter, where 90% of the signal is reflected towards the characterization setup. After filtering reflected laser excitation with a longpass filter (Semrock BLP01-635R), a motorized flip-mirror allows automatic switching between a free space avalanche photodiode (Excelitas SPCM-AQRH-14) and other characterization equipment. The APD counts are recorded by a data acquisition digital-analog converter (National Instruments USB-6343) and synchronized to the laser pulses via the pulseblaster. In particular, because our longpass filter also blocks the coherent ZPL emissions along with the laser, we use the APD to collect the NV phonon sideband (PSB), the red-detuned emissions resulting from phonon emission during excited state decay. A motorized half waveplate ($\lambda/2$) and polarizing beamsplitter allow automatic switching between a spectrometer (Princeton Instruments Isoplane SCT 320) and a fiber-based Hanbury Brown and Twiss (HBT) interferometer consisting of a fiber beamsplitter (Evanescent Optics) and two fiber-input APDs (Excelitas SPCM-AQRH-14-FC and Perkin Elmer SPCM-AQRH-14-FC). The former enables 40 pm resolution characterization of the NV ZPL; the transitions themselves are around 1 pm or less in width, so the spectrometer is merely used to find the coarse transition wavelengths. The HBT interferometer enables second-order autocorrelation measurements with a picosecond resolution time tagger (PicoQuant PicoHarp 300).

For microwave delivery, two signal generators (Rohde & Schwarz SMIQ03B and SMV03) are fed through individual switches (Mini-Circuits ZASWA-2-50DR+), which are gated by the pulseblaster. The outputs of these switches are combined and sent through an amplifier (Mini-Circuits ZHL-16W-43+) before connecting to a feed-through built into the cryostat wall, allowing delivery of microwaves to the inside of the chamber, even while at vacuum and cryogenic temperatures. A central control computer interfaces with hardware as indicated in Figure 3-1 and both issues commands and collects data.

3.2 Sample

Most quantum information experiments performed with diamond defect centers use samples specially selected to have low strain environments, such as natural or chemical vapor

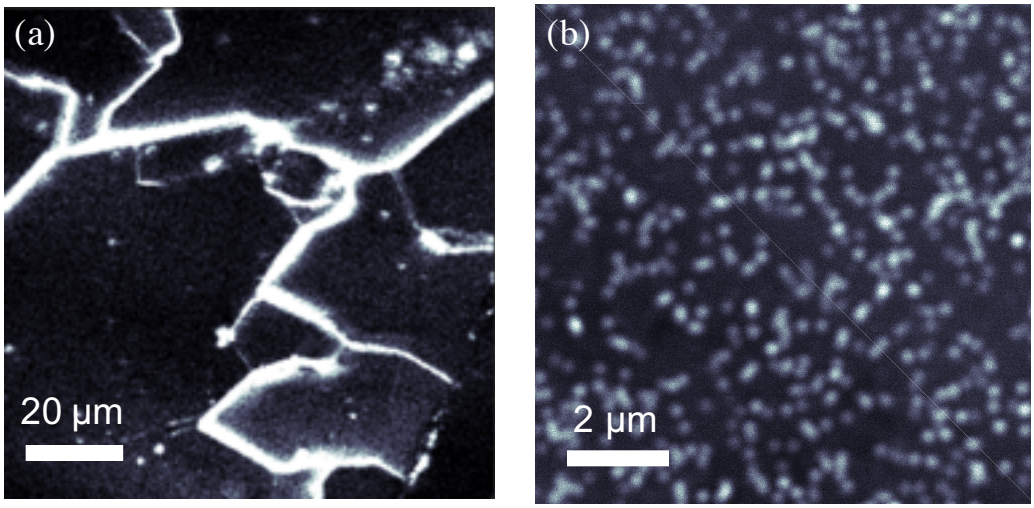

Figure 3-2: (a) A large field-of-view confocal scan of a PCD under 532 nm illumination. The bright lines are boundaries between single crystal grains. (b) Higher resolution scan showing clearly resolvable single defects, as well as clusters with multiple NVs below the diffraction limit.

deposition (CVD) grown single crystal diamonds, such that the inhomogeneous broadening of NV ZPLs is relatively low. Our application seeks the opposite, as high strain environments will enhance the resonance splitting between nearby NVs. Polycrystalline diamonds (PCD) [34] are comprised of multiple grain regions, with large $\sim$10 μm single crystal regions that meet in highly strained boundaries, easily seen in fluorescence microscopy (Figure 3-2a). Each grain has distinct properties, with variable natural defect densities between grains ranging from nearly IIa-like (where single defects are not resolvable) to low density with clear single defect sites, like that shown in Figure 3-2b. The high strain and range of NV densities provide an ideal environment for our experiments, giving us access to both single NVs and clusters. We use a PCD produced by CVD (Element Six) with a native nitrogen concentration of $<$50 ppb. To increase the prevalence of sub-diffraction clusters, the sample is implanted with nitrogen at 85 keV with a density of 10^{10} cm^{-2}, and subsequently annealed at 1200°C for 8 hours to heal the lattice and facilitate the formation of NV centers.

To efficiently deliver microwaves to the sample, we fabricate gold striplines on the surface of the diamond using the following protocol:

1. Solvent clean, sonicating the sample in acetone, methanol, isopropyl alcohol (IPA), and water for 5 minutes each

2. Oxygen plasma clean at 100 W for 5 minutes

3. Spin-coat ZEP resist at 6 kRPM to achieve a target thickness of 200 nm

4. Write electron-beam patterns at 2 nA current, with a dose of 640 μC cm^{-2}

5. Develop in ortho-xylene at room temperature for 10 seconds

6. Deposit 5 nm of chrome for adhesion, followed by 100 nm of gold

7. Sit overnight in N-Methyl-2-pyrrolidone (NMP)

8. Remove any remaining resist with sonication in IPA

The stripline pattern is a simple loop, with ends that taper out to large bonding pads. The design parameters sweep wire widths and gap sizes as shown in Table 3.1, with lengths chosen such that the longest stripline of each width would have resistance below 20 Ω. Figure 3-3a shows the full design pattern; the wires on a given side share a common width and different gap sizes, with the longest wires having the largest gaps to prevent premature shorting. Figure 3-3b shows a camera image of a few of these striplines post-fabrication.

Connections between these striplines and the microwave electronics outside of the cryostat add an additional heat load, making it undesirable to connect more striplines than necessary. Pre-characterizing the optical properties within each stripline allows us to select the most promising region for further experiments. The area chosen is boxed in Figure 3-3a, shown in confocal imaging in Figure 3-3c, and has its entry bolded in Table 3.1. This region was selected based on NV density, showing both clear single NVs and clusters in good proximity to the wire. The sample is silver pasted to a piece of quartz with long tapered gold leads,

		Width			
		5 μm	10 μm	20 μm	30 μm
Gap	30 μm	**16.1** Ω	15.8 Ω	15.6 Ω	15.5 Ω
	20 μm	12.3 Ω	11.6 Ω	11.1 Ω	10.9 Ω
	15 μm	8.3 Ω	7.2 Ω	6.6 Ω	6.3 Ω
	10 μm	4.0 Ω	2.7 Ω	2.0 Ω	1.7 Ω

Table 3.1: Design parameters for gold striplines. Lengths were chosen such that the longest wire at each width (corresponding to the largest gap size) would have resistance near 16 Ω.

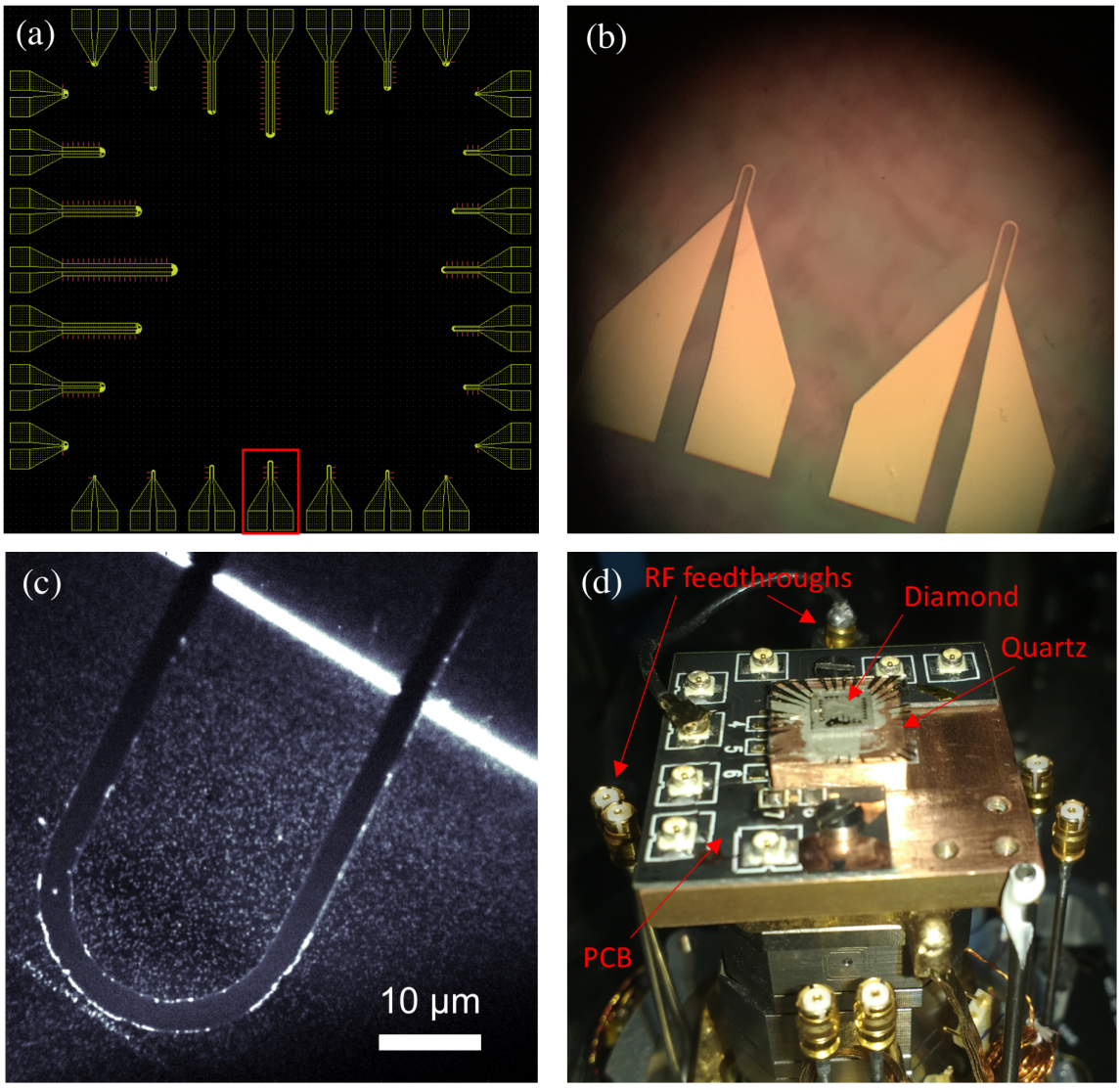

Figure 3-3: (a) GDS schematic of stripline pattern, showing sweeps in wire width, length, and gap size, covering a 4 mm by 4 mm center area of the full 5 mm by 5 mm PCD. Boxed in red, the stripline shown in (c) used for the experiments discussed in this work. (b) Camera image of striplines post-fabrication. (c) Confocal image (532 nm illumination) of a stripline on a region with both single NVs and clusters. (d) Mounting for the sample, showing the diamond, quartz piece with leads, PCB, and connections to RF feedthroughs.

which are wire bonded to the pads of the stripline. The quartz is further silver pasted to a custom copper mount; this mount has a raised center to bring the sample closer to the microscope objective while still providing room for additional circuitry on the mount edges. Here we place a custom printed circuit board (PCB) that lets us go from wire bonding pads to more standard connectors in our cryostat. The quartz leads are wire bonded to the PCB pads, and the corresponding SMA port is connected to an RF feed-through line built into the cryostat, giving us access to the internal electronics while the chamber is pumped down to low vacuum and low temperatures. A photograph of this complete mounting can be seen in Figure 3-3d.

3.3 Cluster Identification and Characterization

The experiments performed in the remainder of this chapter are largely conducted using the same cluster of NVs. A number of techniques are available to identify the presence of multiple NV centers within a diffraction-limited spot, and furthermore to determine more precisely the number therein. To first order in an optical microscope, the brightness of a spot as well as the shape (for clusters with separations on the order of the diffraction limit) can give a good indication that a spot may contain multiple NVs. For example, we identify a spot in Figure 3-4a that is both brighter than the typical spots around it and more elliptical in shape, making it a good candidate for further study.

3.3.1 Intensity auto-correlation

Another valuable characterization is a second order autocorrelation measurement, also known as $g^{(2)}$ [40], which we can perform using our HBT interferometer. This interferometer measures the intensity correlation:

$$g^{(2)}(\tau) = \frac{\langle I(t)I(t+\tau)\rangle}{\langle I(t)\rangle^2} \tag{3.1}$$

which has a quantum mechanical analog:

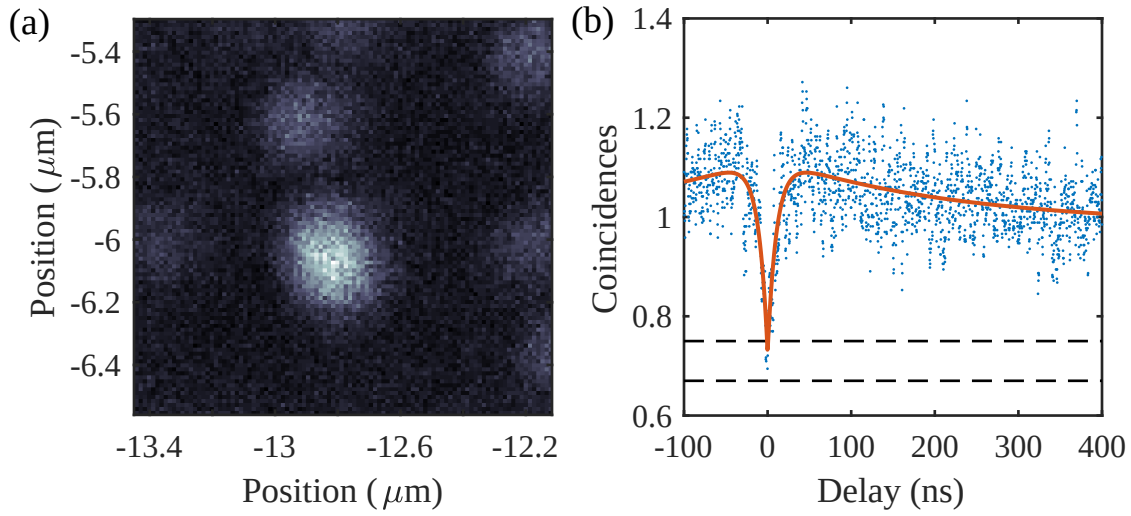

Figure 3-4: (a) Confocal scan under 532 nm excitation, showing one diffraction-limited spot to be much brighter and more elliptical than its neighbors. (b) Second-order autocorrelation $g^{(2)}$; data in blue, fit in red, and dashed lines indicating the 3-emitter and 4-emitter bounds, respectively. No background correction has been performed with these data.

$$g^{(2)}(\tau) = \frac{\langle \hat{a}^\dagger \hat{a}^\dagger \hat{a} \hat{a} \rangle}{\langle \hat{a}^\dagger \hat{a} \rangle^2} \tag{3.2}$$

where $\hat{a}^\dagger$ and $\hat{a}$ are the raising and lowering operators (i.e. photon creation and annihilation operators) of the field. For all realizable light sources, this has the property $g^{(2)}(\infty) = 1$, as for long time scales the intensities become uncorrelated. In the case of a Fock state with a well defined number of photons n, the $\tau = 0$ case simplifies to:

$$g^{(2)}_{\text{Fock}}(0) = 1 - \frac{1}{n} \tag{3.3}$$

One can gain intuition for this expression by considering the quantized nature of photons. The wavefunction of a single photon entering a HBT setup may split at the beamsplitter, with portions of the wave traveling down both interferometer arms. However, since there is only one photon, only one APD can register a detection event, a measurement that collapses the superposition. Thus, monitoring the timing of clicks on both detectors for long periods of times will show that, for a single-photon Fock state, both detectors will not register

detections at the same time. In the experimental case, background fluorescence and detector dark counts can however degrade this, yielding measurements slightly above 0.

The expression above further shows that a two-photon Fock state gives a 50% probability for both detectors to click at the same time (compared to the $\tau \to \infty$ case); similarly, one can see that given the first photon was detected on a certain detector, there is a 50% probability that the second photon will be detected on the other detector, resulting in a coincidence. Note that this implies that any $g^{(2)}(0) < 0.5$ must have come from a single photon source. In general, the location of $g^{(2)}(0)$ creates bounds on the possible number state of the light being measured. Since single atoms emit single photons upon decay, this can in turn create bounds on the possible number of atoms being measured. Performing this measurement on our cluster yields the results shown in Figure 3-4b. Fitting this gives $g^{(2)}(0) = 0.728$, lying between the three emitter bound (0.67) and the four emitter bound (0.75), indicating the presence of no more than 3 emitters.

3.3.2 Spectral characterization

Characterizing the spectral properties of this spot provides a more reliable confirmation of the presence of multiple NV centers. In particular, we perform spectroscopy on 1) the optical dipole transitions and 2) the microwave spin transitions of the system.

Optical spectrum

Recall from Chapters 1 and 2 that an NV center initialized into its $m_s = 0$ ground state should have two excited state transitions available, one into each of the $E_{x,y}$ levels. High strain that strongly breaks the system symmetry can also cause spin mixing, at which point the NV can, in principle, exhibit transitions into as many as six excited states (see Figure 1-1b). These transitions can be characterized through resonant photoluminescence excitation (PLE) spectroscopy. First, we coarsely characterize the transition wavelengths of the NV by exciting with green light and collecting emissions on our spectrometer, yielding the spectrum in Figure 3-5a. Two peaks are observable; these could correspond to either 1) a single highly strained NV, or 2) multiple spectrometer-limited NVs.

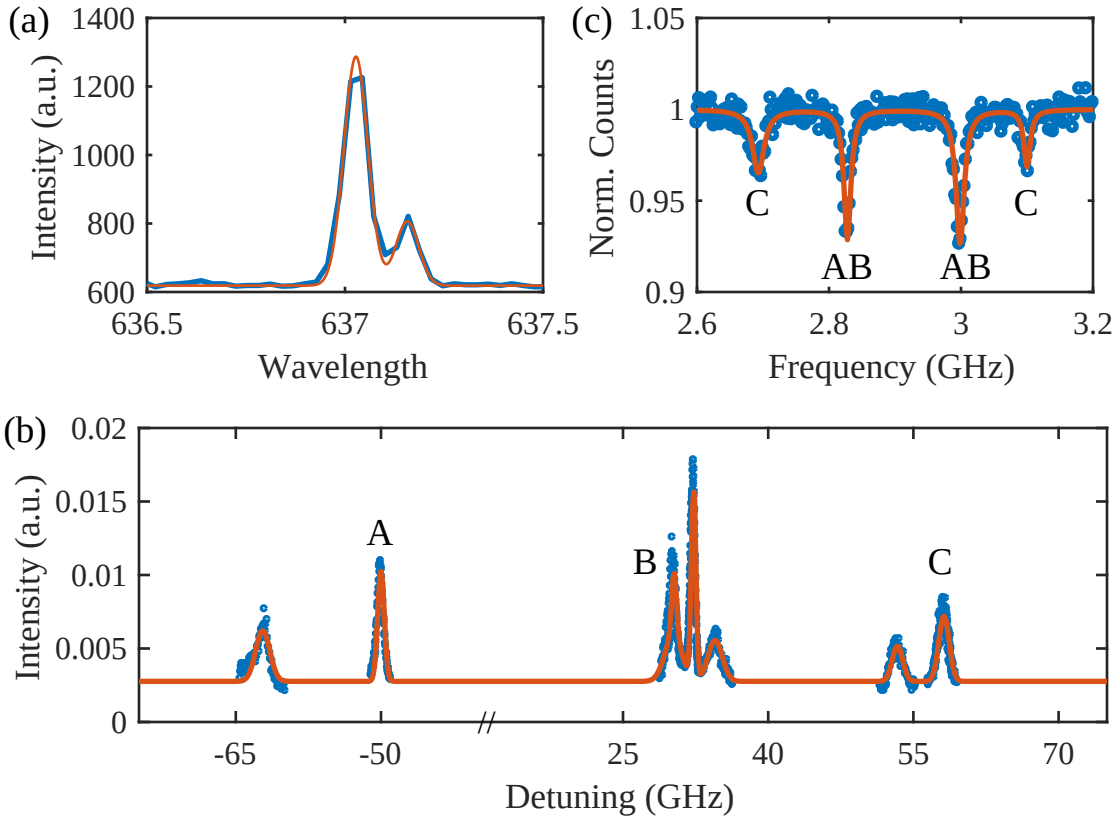

Figure 3-5: (a) Optical spectrum of the NV cluster under 532 nm illumination, with data in blue and a fit to two Gaussians in red. (b) PLE spectroscopy of the cluster, showing seven resolvable ZPL transitions. Data in blue, fit to multiple Gaussians in red. Data plotted as a function of detuning from a center frequency of 470.475 THz. We label three specific peaks for future reference, each corresponding to the most distinguishable peak from a given NV. (c) ODMR spectroscopy of the cluster, indicating two NV orientations within the cluster. Data in blue, fit to four Lorentzians in red. We also label these peaks with the NVs to which they correspond, determined by the mapping performed in Figure 3-6.

Next, to measure PLE, we use a pulse sequence consisting of a 2–5 μs 532 nm pulse to initialize the NV, followed by a 0.5–10 μs pulse from our tunable red laser, with the exact timings depending on the power of each laser. On resonance, the red pulse excites the NV into its excited state, where it can decay and emit photons which we can detect on our APD. However, since the laser frequency sweeps the ZPL transition of the NV, we must use a longpass filter to block out laser reflections, which in turn blocks the coherent NV emissions near 637 nm. Fortunately, the NV center exhibits a low Debye-Waller factor, with only around 3% of its emissions occurring along the ZPL. The remaining 97% is scattered

into a phonon sideband (PSB), where phonon creation lowers the energy and thus raises the wavelength of the emitted photons. Thus, spectral filtering of the laser only removes a small portion of the total fluorescence, allowing us to still use this PLE measurement to characterize the ZPL properties[1]. This sequence is repeated for 10^4–10^5 averages at a single frequency, then the laser is moved to the next frequency and the sequence repeated. A wavemeter continuously measures the red laser frequency and provides feedback to stabilize and lock the frequency with 10 MHz precision. These data are shown in Figure 3-5b; the presence of seven peaks indicates that we have at least two NVs (as strong strain-induced mixing would produce at most six transitions per NV), and no more than 3 NVs (as the minimally strained case would produce at least two transitions per NV).

Microwave spectrum

In addition to characterizing the ground-excited state optical transitions, we can also characterize the ground state spin transitions by performing optically detected magnetic resonance (ODMR) spectroscopy. As discussed in Section 1.1.1, the NV's $m_s = \pm 1$ ground states give off less average fluorescence under 532 nm excitation than the $m_s = 0$ state due to coupling to a metastable singlet state. This can be used to probe the transitions of the ground state spin transitions. We simultaneously apply a microwave (MW) tone near 2.9 GHz and excite the system with green light while monitoring the fluorescence. Near resonance, the microwaves will shift some population into the $m_s = \pm 1$ states, resulting in net lower fluorescence. This fluorescence is normalized to a measurement under no MW excitation, corresponding to the $m_s = 0$ bright state fluorescence. For our particular implementation, we apply a static external magnetic field, where the axial component will split the $m_s = +1$ and $m_s = -1$ levels, allowing us to address each individually. This so-called CW ODMR spectroscopy is shown in Figure 3-5c. Because the magnitude of the spin ± 1 splitting is proportional to the axial projection of the applied magnetic field, NVs of different orientations may experience different splittings dependent on the field alignment. Our results show at most four dips, corresponding to two NV orientations being present within this cluster.

[1]Another technique for separating the excitation laser from the NV emissions is to use a polarization scheme, where the excitation laser is slightly off-axis from the NV, allowing separation of the two by the use of a half-waveplate and a linear polarizer [37].

Furthermore, we note that one pair of dips is roughly twice as pronounced as the other, suggesting that we may have two NVs in one orientation, and one in the other.

Mapping between optical and microwave transitions

The combined observations made up to this point strongly suggest the presence of three NVs in this cluster. However, in order to have both individual control and individual read-out of each single NV, we must determine which optical transitions and which microwave transitions correspond to the same NVs. To do this, we induce Rabi oscillations by applying microwaves at one of the ODMR frequencies ω_i for a time τ, then reading out the state of the NV with ZPL frequency ν_j by monitoring the fluorescence while applying a short (300 ns) pulse with the red laser locked to ν_j. We repeat this for every combination of ω_i and ν_j. In each instance, if ω_i and ν_j correspond to the same NV, we expect to see a modulation of the observed fluorescence as we vary τ, as an NV is driven out of its $m_s = 0$ state then excited on the $m_s = 0$ ZPL transition. If, however, ω_i and ν_j correspond to different NVs, there should be no modulation, as the NV being driven by ω_i is not the same as that being read out by ν_j. This fluorescence is again normalized to a measurement after no MW excitation.

The data for each combination are shown in Figure 3-6, with MW frequencies by column and ZPL frequencies by row. Since an NV cannot have more than two MW transitions, some data were not taken after it was clear which MW transitions were associated with a given ZPL; these plots are left blank. The plots are also color coded by result type. Green indicates negative contrast, which is expected for the case where ω_i and ν_j correspond to the same NV and ω_i is a $m_s = 0$ transition into one of E_x, E_y. Red indicates no contrast, expected for the case where ω_i and ν_j correspond to different NVs. Blue indicates positive contrast; while this does suggest that ω_i and ν_j correspond to the same NV, it is unusual, as it indicates ν_j is driving the NV into a state that is more likely to be excited by ω_i. One explanation is that ω_i is not a transition into one of the $m_s = 0$ excited state levels, but is rather a spin-mixed transition, such that spin driving at ν_j moves more population into a level that can be excited by ω_i. These data thus confirm and clarify the results of previous sections: our system consists of three NVs, two of which are aligned in the same direction, and one of which is aligned to a different direction. Furthermore, the PLE resonances correspond

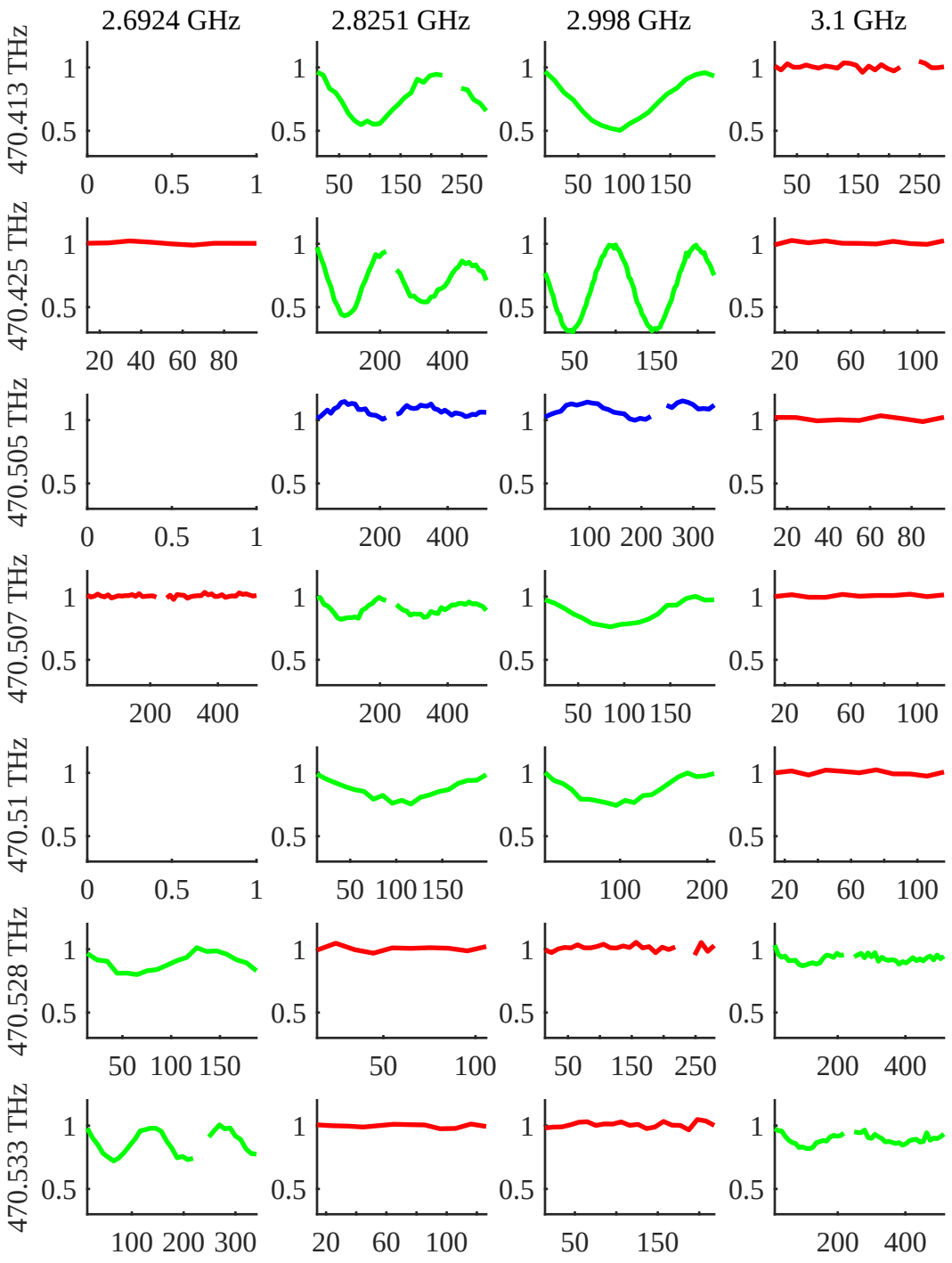

Figure 3-6: Results of Rabi experiments with each MW (column) and optical (row) frequency combination. x-axes are MW time τ in nanoseconds, y-axes are normalized fluorescence. Green = negative contrast, confirmation of $m_s = 0 \rightarrow \pm 1$ driving. Red = no contrast. Blue = positive contrast, indicating a possible spin-mixed transition.

largely to the expected E_x/E_y transitions, with one additional resonance from a strongly spin-mixed transition.

3.3.3 Optical Rabi characterization

The optical Rabi frequency is a critical component of this work, and while our lab infrastructure does not enable direct measurement of the optical Rabi frequency via fast time gating of the optical pulse, we can measure it indirectly through saturation measurements. The steady-state emission from a two level system has a Lorentzian frequency profile as follows from Equation 2.7. Experimentally, the measured fluorescence as a function of excitation power when on resonance will be dependent on loss, the dipole moment of the transition, and background noise. This is captured in the following model:

$$F = 2E\frac{CP\gamma}{\gamma^2 + 4CP} + BP \tag{3.4}$$

where E is the total efficiency of the setup including all losses and detector inefficiencies, C is a conversion constant between laser power and Rabi frequency that accounts for the dipole moment and orientation as well as any losses on the excitation path, P is the laser power, and B is a constant for the power-dependent background fluorescence that includes the losses contained in E. In our setup, detector dark counts and non-laser induced background are low enough to neglect.

To fit this model, we perform resonant PLE spectroscopy at varying laser powers on a well-isolated single NV, measuring the peak fluorescence at resonance. For these PLE measurements, we use a pulse sequence consisting of a 5 μs 532 nm pulse to initialize the NV, followed by a 500 ns pulse from our tunable red laser, during which time we record fluorescence counts. This is repeated for 10^5 averages at each frequency point. These raw data and their Lorentzian fits are shown in Figure 3-7a.

In order to better constrain the fit of the saturation curve, we fix $\gamma = 670$ MHz, the effective linewidth retrieved from fitting the individual Lorentzians at low powers, where the line should not be power broadened. As a result, we need only fit the efficiency E, the power-to-Rabi conversion factor C, and the background rate B, determined to be:

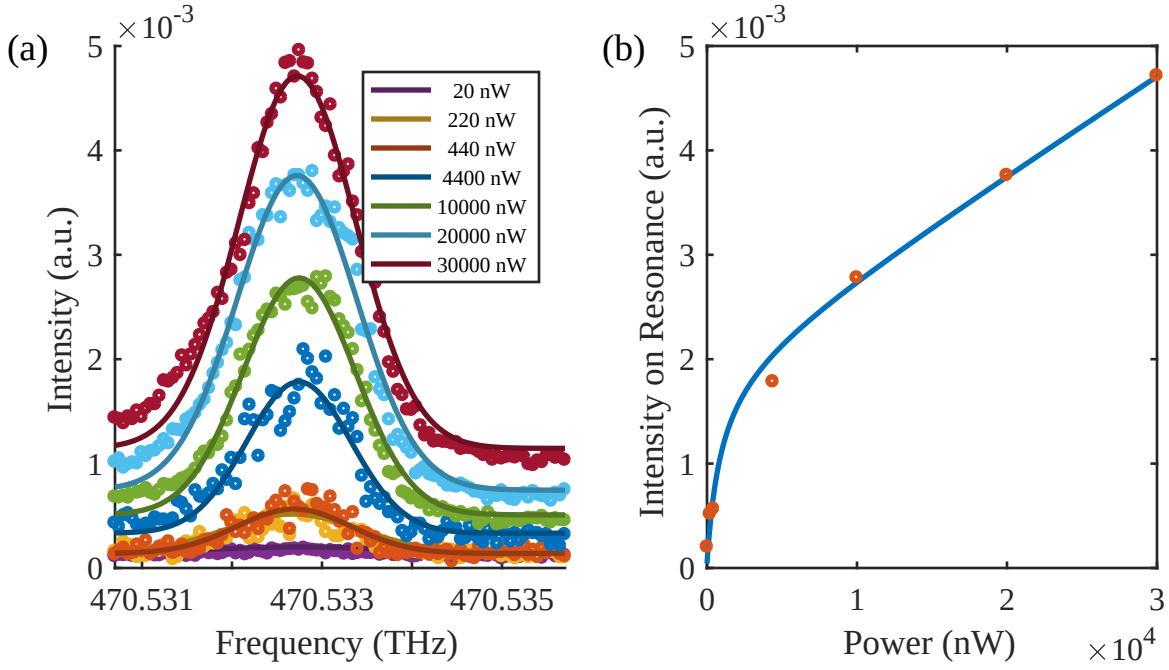

Figure 3-7: (a) PLE scans for varying excitation powers. (b) The peak values after fitting as a function of laser power (red dots), enabling fitting of the model in Equation 3.4 (solid blue).

$$E = 0.678\%$$

$$C = 91.7 \text{ GHz}^2/\text{mW}$$

$$B = 93.3 \text{ MHz/mW}$$

The resulting curve of which is plotted alongside the data in Figure 3-7b. Note that while this fit incorporated a fixed linewidth, the Rabi frequency is dependent on the field intensity and the dipole moment; thus, this conversion factor will hold for future measurements for any NV of the same orientation.

To summarize, the measurements in this section have allowed us to identify a cluster of 3 NV centers. Spin resonance (ODMR) measurements allow us to characterize their orientations and determine the MW frequencies that can be used to individually control each qubit. Optical resonance (PLE) measurements allow us to determine the ZPL frequencies

that can be used to read out each qubit. Saturation measurements on these optical resonances further give us insight into how much optical driving is being applied for a given optical power, with the equivalent measurement for the MW power given by the Rabi measurements described above. This set of tools enables the experimental applications discussed in the remainder of this chapter.

3.4 Super-Resolution Localization

As discussed in Section 2.2.1, non-degenerate transitions like those observed in our NV cluster can be used to preferentially induce fluorescence from individual emitters by applying a narrow resonant laser. For sufficiently large detunings, this enables imaging of essentially a single NV. Since a single emitter in a known optical system has a well-known point spread function, it is possible to localize this emitter with arbitrary precision. In our implementation, this will be limited by 1) imperfect preferential imaging stemming from finite detunings, and 2) stage drift.

3.4.1 Protocol

To perform the localization, the red laser is locked to one of the resonant frequencies ν_i. We then raster scan across the sample, performing a single-frequency PLE measurement at each pixel. This is the exact same pulse sequence as that described above. Repeating this for each ν_i yields the results in Figure 3-8, shown next to a 532 nm confocal scan of the same region for comparison. Note that the relative fluorescence between the 532 nm and ZPL scans should not be compared, as the integration times and count rates are different between these two measurement types.

After taking these images, a symmetric 2D Gaussian fit determines the emitter position, with free parameters $\{A, x_0, y_0, \sigma, D\}$ under the model:

$$F = Ae^{-(x-x_0)^2-(y-y_0)^2/2\sigma^2} + D \tag{3.5}$$

An example of this fit process is shown in Figure 3-9. This process lets us formally con-

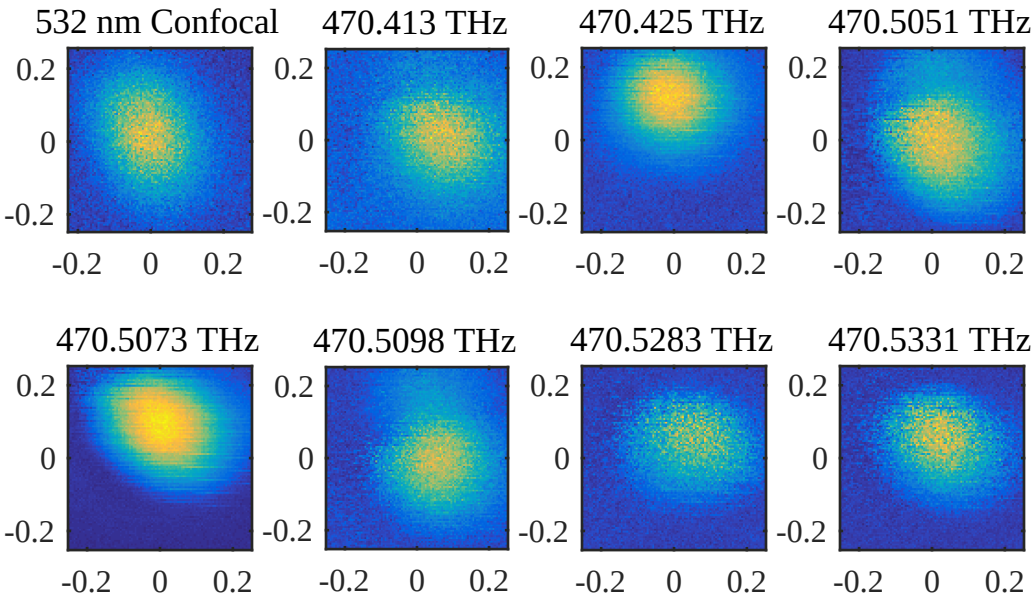

Figure 3-8: Comparison between the confocal scan under 532 nm excitation (top left) and the super-resolution PLE scan under excitation at each ZPL frequency. Axes are position in μm.

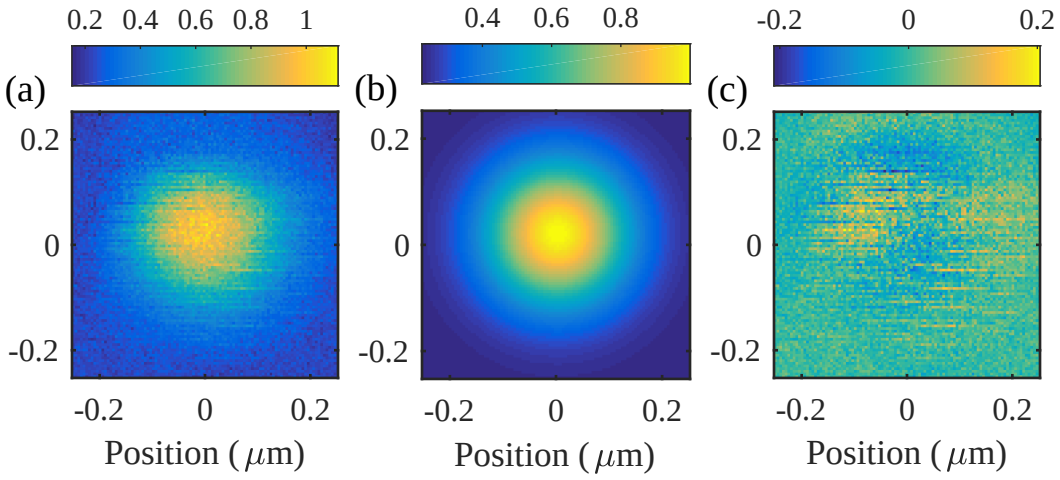

Figure 3-9: Fitting process for super-resolution localization. All color map data are normalized to the same value, the fitted peak height, such that the scaling of the residuals in (c) is fractional error. (a) Super-resolution image for $\nu_i = 470.425$ THz, recentered. (b) Gaussian fit as per Equation 3.5. (c) Residuals between fit and data, with mean value of $7.9 \times 10^{-7}\%$ and RMS error of 4.2%.

firm that three ZPLs (470.413, **470.5051**, and 470.5098 THz) correspond to a single NV, two ZPLs (**470.425** and 470.5073 THz) correspond to a second NV of the same orientation, and the final two ZPLs (470.5283 and **470.5331** THz) correspond to a third NV at a different orientation. Due to differing transition strengths and differing proximity to adjacent transitions, some of the ZPLs are able to produce better localization results than others; we thus select the best ZPL from each NV for further analysis, labeled A, B, and C in Figure 3-5b and bolded in the lists at the beginning of this paragraph.

3.4.2 Analysis

The localization precision of each emitter can be taken to be the 95% confidence interval on the fit center. However, to more conservatively estimate our precision in a manner that reflects a realistic implementation, we repeat the localization experiment 69 times over a period of around 20 hours, taking the spread on these measurements to be our true localization precision. The results of these individual trials are shown in Figures 3-10a, with the color gradient indicating relative time of each datapoint. As the data from each of the three NVs are well separated and clusters easily identifiable by eye, we plot each with the same color scheme.

Examining the temporal trend for each NV, it is readily apparent that there is some uniform drift on our stage over the course of the measurement period. In Figure 3-10b, for each NV, we plot the difference in x-coordinate and y-coordinate between the fit center at time t and that at time $t = 0$. Both x and y follow clear trends, and linearly fitting these drifts allows us to compensate by shifting each datapoint's center according to the fitted drift for that time point. This adjustment results in the localization image shown in Figure 3-10c, clearly showing much tighter clustering than Figure 3-10a.

From these data, we extract the standard distance, i.e. standard error in position, for each NV:

$$S(N) = \sum_{i=1}^{N} \sqrt{\frac{(x_i - \bar{x})^2 + (y_i - \bar{y})^2}{N}} \tag{3.6}$$

where each i is one of the 69 trials and $\bar{x}$ and $\bar{y}$ are mean positions of the total dataset (for

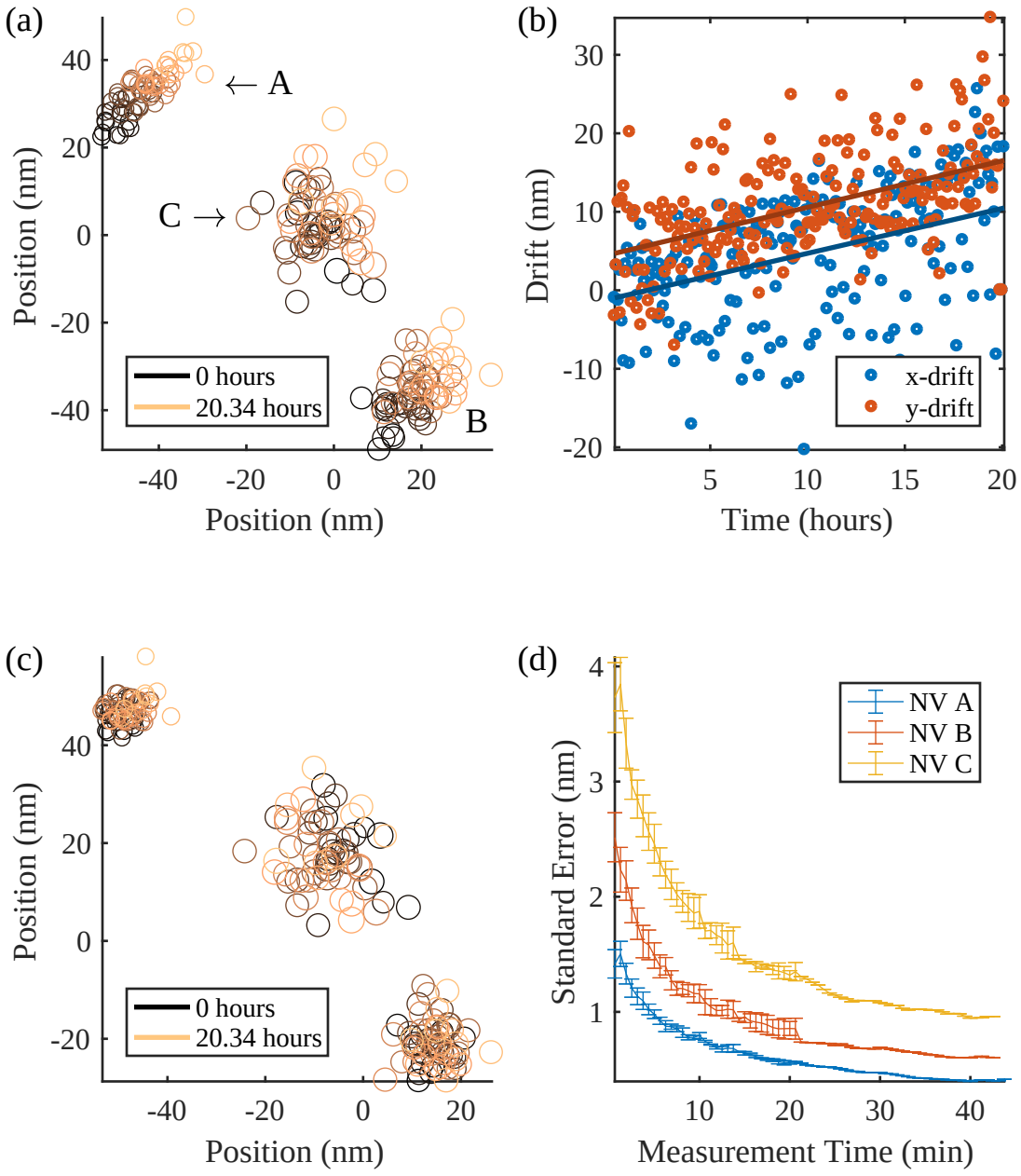

Figure 3-10: (a) Results of 69 super-resolution localization trials for each NV, with color representing the time at which the measurement was taking. Different NVs labeled by convention used above, and are given the same color scale, as the clusters are separated enough to distinguish by eye. Sizes of circles are in arbitrary units, but are scaled to indicate 95% confidence intervals on each measurement. (b) Drift of all three NVs in x (blue) and y (red) over the measurement period, overlaid with linear fits. (c) Data from (a), with drift compensated according to the fits in (b). (d) The standard error as per Equation 3.6 for each NV as a function of total measurement time.

a given NV). We calculate S for every sequential binning of N trials, with N running from $N = 1$ to $N = N_{max} = 69$. Figure 3-10d plots the mean standard error as a function of total measurement time given by $T = Ndt$, where $dt = 37.5$ seconds is the total pulse sequence time for a single measurement. Error bars indicate the standard error on the calculation of each $S(N)$. From these results, we demonstrate localization of single NV centers to a mean precision of 0.647 nm.

3.5 Individual Control and Readout

While the above application demonstrates the steady-state fluorescence difference between detuned emitters, our theory (Eq. 2.11) predicts that for sufficiently short excitation times and large detunings, the off-resonant qubit will with high probability (as plotted in Fig. 2-4) experience no bit-error inducing decay events. This feature should enable individual readout of NV centers in a manner that keeps the quantum states of nearby centers protected, both in population and in phase.

3.5.1 Ramsey interferometry

We explore these dynamics using Ramsey interferometery, which is best understood using Bloch vector formalism:

$$\begin{bmatrix} x \\ y \\ z \end{bmatrix} = \begin{bmatrix} \rho_{10} + \rho_{01} \\ i\left(\rho_{10} - \rho_{01}\right) \\ \rho_{11} - \rho_{00} \end{bmatrix} \tag{3.7}$$

An NV initialized in the $m_s = 0$ ground state $|\psi\rangle_0 = |0\rangle$ is coherently driven by microwaves, rotating the state around the y-axis[2] by $\frac{\pi}{2}$ radians (referred to henceforth as a $\frac{\pi}{2}$-pulse):

[2]As long as one maintains consistency in future operations, the choice of y-axis vs. x-axis is arbitrary up to a global phase; we choose y here for notational simplicity.

$$R_y\left(\frac{\pi}{2}\right)|\psi\rangle_0 = \begin{bmatrix} 0 & 0 & 1 \\ 0 & 1 & 0 \\ -1 & 0 & 0 \end{bmatrix} \begin{bmatrix} 0 \\ 0 \\ -1 \end{bmatrix}$$
$$|\psi\rangle_1 = \begin{bmatrix} -1 \\ 0 \\ 0 \end{bmatrix} \tag{3.8}$$

Note that we are working in the rotating frame of the microwaves at ω_0. In this state, hyperfine couplings to the nuclear spin of the nearby nitrogen will cause the $|1\rangle$ component to pick up phase relative to the $|0\rangle$ component. It is clear from Equation 3.7 that this phase manifests as a rotation about the z-axis. The functional form of this phase evolution will depend on the number of hyperfine levels, as well as their detuning $\delta\omega$ from the driving frequency ω_0; in particular, each hyperfine level should pick up a $\delta\omega \cdot \tau$ phase after a free precession time τ. We abstract these away for notational purposes and write a generalized phase gate $R_z\left(\theta(\tau)\right)$:

$$R_z\left(\theta(\tau)\right)|\psi\rangle_1 = \begin{bmatrix} \cos\left(\theta(\tau)\right) & -\sin\left(\theta(\tau)\right) & 0 \\ \sin\left(\theta(\tau)\right) & \cos\left(\theta(\tau)\right) & 0 \\ 0 & 0 & 1 \end{bmatrix} \begin{bmatrix} -1 \\ 0 \\ 0 \end{bmatrix}$$
$$|\psi\rangle_2 = \begin{bmatrix} -\cos\left(\theta(\tau)\right) \\ -\sin\left(\theta(\tau)\right) \\ 0 \end{bmatrix} \tag{3.9}$$

Finally, a second $\frac{\pi}{2}$-pulse around the y-axis, another $R_y\left(\frac{\pi}{2}\right)$ gate, is now applied:

$$R_y\left(\frac{\pi}{2}\right)|\psi\rangle_2 = \begin{bmatrix} 0 & 0 & 1 \\ 0 & 1 & 0 \\ -1 & 0 & 0 \end{bmatrix} \begin{bmatrix} -\cos(\theta(\tau)) \\ -\sin(\theta(\tau)) \\ 0 \end{bmatrix}$$
$$|\psi\rangle_f = \begin{bmatrix} 0 \\ -\sin(\theta(\tau)) \\ \cos(\theta(\tau)) \end{bmatrix} \tag{3.10}$$

The Ramsey interferometry sequence concludes by measuring the population difference; for the NV this is simply done by applying 532 nm light and measuring the fluorescence, which due to the mechanisms discussed in Section 1.1.1 directly corresponds to $\rho_{11} - \rho_{00}$ after normalization. From this, we can see that a single hyperfine level, with $\theta(\tau) = \delta\omega\tau$, would result in a normalized fluorescence of $\cos(\delta\omega\tau)$; by extension, each hyperfine level adds an additional sinusoidal term based on its detuning from the microwave source.

Effect of crosstalk-induced decay

The above formalism did not account for any sources of decoherence, which manifests as an exponential decay envelope on the sinusoidal oscillations. More importantly for our applications, it also presumes that phase evolution is the only dynamic during the free precession interval. Our scheme proposes the introduction of a laser that may induce spontaneous decay events. We can modify the density matrix appropriately to reflect this mixed state. After the free precession interval, our system is in the partially mixed state[3]:

$$\rho_2 = \frac{\eta}{2}\begin{bmatrix} 1 & i\sin(\theta(\tau)) - \cos(\theta(\tau)) \\ -i\sin(\theta(\tau)) - \cos(\theta(\tau)) & 1 \end{bmatrix} + (1-\eta)\begin{bmatrix} 1 & 0 \\ 0 & 0 \end{bmatrix} \tag{3.11}$$

where η is the probability of experiencing no decay events as per Equation 2.11. While the

[3]Here, we assume that the primary channels for excitation and subsequent decay are the $m_s = 0$ ground-excited transitions; in practice, this can occur for the $m_s = \pm 1$ transitions as well. However, as the post-decay state will still be fully mixed as shown here, the end result after the $R_y\left(\frac{\pi}{2}\right)$ and measurement gates will be identical.

action of the subsequent $R_y\left(\frac{\pi}{2}\right)$ gate on the first term is described above in Equation 3.10, its effect on the second term is in fact identical to that of our first $R_y\left(\frac{\pi}{2}\right)$ gate (Equation 3.8). The final density matrix is thus:

$$\rho_f = \frac{\eta}{2}\begin{bmatrix} 1-\cos\left(\theta(\tau)\right) & i\sin\left(\theta(\tau)\right) \\ -i\sin\left(\theta(\tau)\right) & 1+\cos\left(\theta(\tau)\right) \end{bmatrix} + \frac{(1-\eta)}{2}\begin{bmatrix} 1 & -1 \\ -1 & 1 \end{bmatrix} \tag{3.12}$$

A measurement of the population difference $\rho_{11} - \rho_{00}$ via normalized fluorescence now yields:

$$\begin{aligned} F &= \frac{\eta}{2}\left[1+\cos\left(\theta(\tau)\right)\right] + \frac{(1-\eta)}{2} - \frac{\eta}{2}\left[1-\cos\left(\theta(\tau)\right)\right] - \frac{(1-\eta)}{2} \\ &= \eta\cos\left(\theta(\tau)\right) \end{aligned} \tag{3.13}$$

Crosstalk will thus directly degrade the fringe amplitudes in this measurement, providing a direct measurement of η that we can use to both confirm our theory and characterize the potential of our system for individual readout.

3.5.2 Single NV crosstalk measurements

A spatially well-isolated single NV center is an ideal system for studying the above dynamics. After identifying the ZPL frequencies via resonant PLE spectroscopy, we perform Ramsey interferometry using the pulse sequence shown in Figure 3-11a. A 5 μs 532 nm pulse initializes the state. Next, a 20 ns MW pulse performs a $\frac{\pi}{2}$ rotation, followed by a free precession period τ and a second $\frac{\pi}{2}$-pulse. A 50 ns red pulse near 637 nm at detuning Δ from the central ZPL transition is centered between the MW pulses. The final state is read by collecting fluorescence for the first 300 ns of a 5 μs 532 nm pulse, which also reinitializes the NV state. A subsequent repetition of this measurement thus gives a reference for the $|0\rangle$ fluorescence that can be used for normalization by dividing the mean photon counts from measurement bin by the mean counts from the reference bin.

Repeating this sequence many times at varying detunings and sweeping the precession period yields the results shown in Figure 3-11b, plotted alongside a reference Ramsey mea-

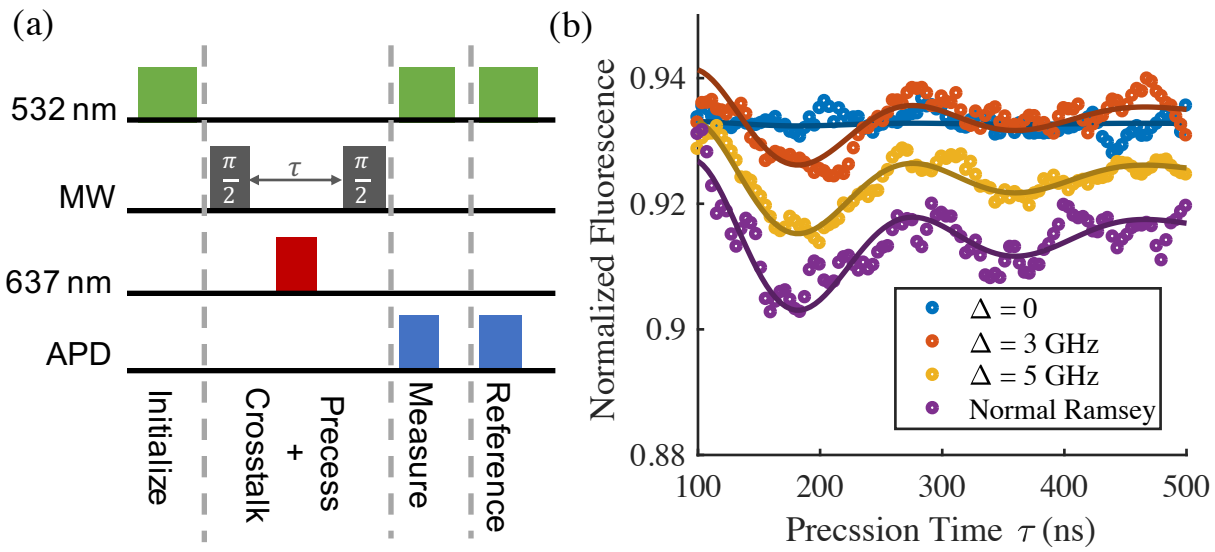

Figure 3-11: (a) Pulse sequence used to measure the effects of a near-resonant laser pulse on a superposition state. (b) Data and associated fits from the pulse sequence in (a) for various detunings of the red laser, alongside a reference Ramsey taken with no red laser pulse during the precession period.

surement taken with no red laser pulse. The reference measurement is fit with the model discussed above of three sinusoids with a decaying envelope, along with an offset to account for the fluorescence of the decayed state for $\tau \to \infty$. The crosstalk measurements are then fit to this same model, but holding constant the frequencies, phases, and relative amplitudes of the sinusoids, along with the decay constant of the envelope. The only fit parameters are thus the overall magnitude of the fringes and the magnitude of the offset, which may differ as the fully mixed state from Equation 3.13 may have a different mean fluorescence compared to the decayed state from a normally decohering Ramsey. As expected, we observe degradation in the fringe amplitude near resonance, gradually recovering contrast as the detuning increasing.

To map out this decay more quantitatively, we repeat this pulse sequence but with the precession time fixed to $\tau = 184$ ns, the time corresponding to the maximal fringe contrast. This allows us to take data at many more detunings and map out the model derived in Equation 2.11. The raw normalized results from these measurements are shown in Figure 3-12a. The expected functional form as plotted in Figure 2-4 is clearly visible; however, to more concretely map this fluorescence onto a bit error rate, we normalize these data to the

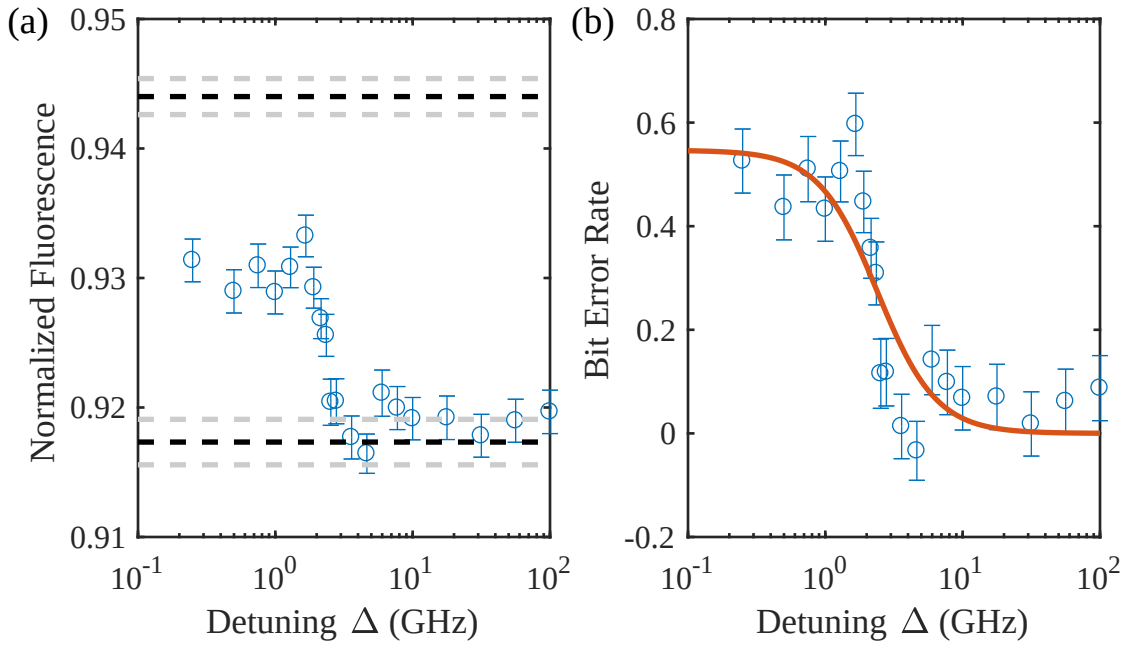

Figure 3-12: (a) Normalized fluorescence for the Ramsey sequence in Fig. 3-11 with fixed $\tau = 184$ ns, corresponding to the deepest fringe. In black dashed lines, the normalization fluorescence levels for the no error and full error cases respectively, each with 95% confidence bounds in gray. (b) Bit error rate after transforming the data in (a) as per Equation 3.14. In red, the theory curve with fixed γ and Ω and only one fit parameter for the exact excitation time T.

no error case, determined by the fringe contrast with no red laser pulse, and the 100% error case, determined by the fluorescence after performing a single $\frac{\pi}{2}$-pulse, which reproduces the same fluorescence as a fully mixed state via our derivation above. These fluorescence levels and their 95% confidence bounds are also included in Figure 3-12a. Simply shifting the data and normalizing by the difference gives the equivalent bit error rate for each detuning datapoint:

$$\text{Error Rate} = \frac{F_{\text{data}} - F_{\text{no error}}}{F_{\text{full error}} - F_{\text{no error}}} \tag{3.14}$$

yielding the data shown in Figure 3-12b, which can now be compared to our theoretical predictions. As derived in Equation 3.14, the bit error rate should follow the form:

$$\text{Bit Error Rate} = 1 - \eta = 1 - e^{-\gamma|\Omega|^2 T/2(|\Omega|^2+\Delta^2)} \tag{3.15}$$

The NV emitter lifetime γ is well known based on pulsed lifetime measurements. Furthermore, the saturation measurements from Section 3.3.3 provide an estimate of the optical Rabi frequency. In principle, the only remaining variable, the excitation time T, is known based on the pulse sequence parameters. However, in practice, the certainty on this value is low due to the relatively slow on-off response time of our AOM. Thus, we fit the model to the data with a single free parameter for this excitation time. The resultant fit shown in Figure 3-12b yields remarkable agreement with our data. These results thus allow us to estimate the detuning required for a given desired crosstalk fidelity.

3.5.3 Simultaneous control and readout

With this knowledge in mind, we use the cluster examined earlier to demonstrate simultaneous control and individual readout on multiple NVs within a diffraction-limited spot. Due to the experimental limitation of only having one red laser that takes milliseconds to frequency tune, we can only perform individual readout on one ZPL. NV C, being alone in its orientation, is a convenient choice, as it allows us to treat NVs A and B as a combined spin register, where both spins are controlled by the same MW frequency and read out together with 532 nm excitation. This also means our Ramsey should be performed on NVs A and B to demonstrate their resilience to readout of NV C. To demonstrate dual control along with readout, we also coherently drive NV C at its own spin resonance to induce Rabi oscillations. The logical gate sequence and its corresponding pulse implementation can be seen in Figure 3-13.

After 532 nm initialization, the spin of NV C is coherently driven for a time τ, performing a rotation $R_y(\theta)$, the classic Rabi oscillations. Next, we perform a Ramsey sequence on NVs A and B, reading out NV C in the middle as done in Figure 3-11a, this time with a 300 ns readout pulse. However, the readout of NVs A and B is more complex here due to the presence of an additional signal from the Rabi oscillations on NV C. In order to decouple and read out just NVs A and B, we perform a series of pulses that correspond to a logical equivalent of a standard green readout. This is done by ionizing NV C with a strong resonant pulse for 5 µs. To ensure ionization independent of the state of NV C, we further perform a MW π-pulse on this NV followed by another red pulse. The readout is then concluded

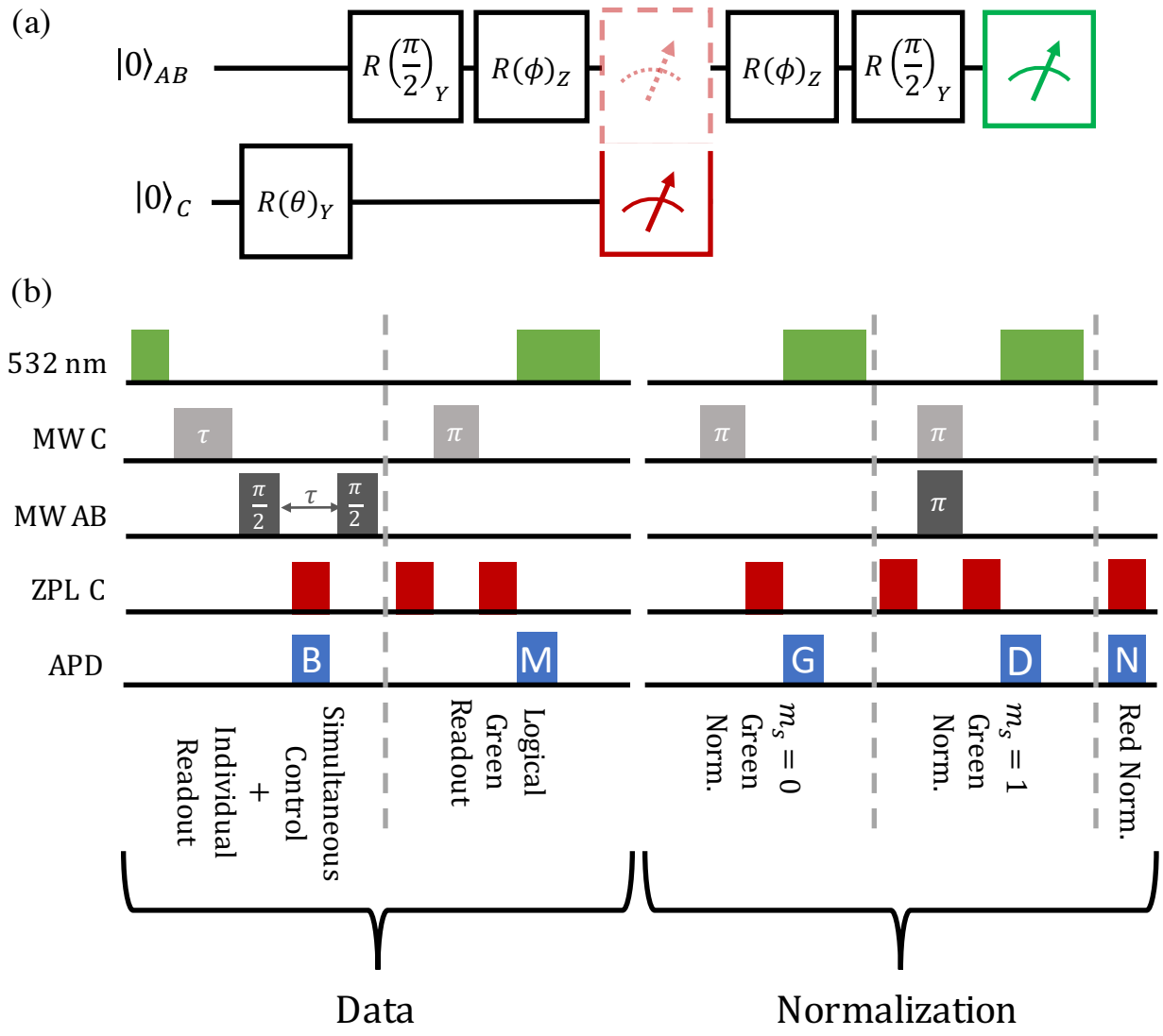

Figure 3-13: (a) Logic gate representation of the pulse sequence used to demonstrate individual control and readout. (b) Sequence as implemented in pulses, showing both the "data" portion of the experiment that corresponds to the logical sequence in (a), and a set of normalization sequences. An additional normalization not shown was performed to measure the Ramsey with no crosstalk; this was identical to the "data" sequence, except without the Rabi pulse τ on NV C (the first bin on the MW C channel) and no readout during the Ramsey precession (the first bin on the ZPL C channel).

by a 5 μs 532 nm pulse, where the first 500 ns are used for photon count collection and the remaining time is used to reionize the system. We follow this sequence by normalization measurements to determine the reference fluorescence levels corresponding to the 1) $m_s = 0$ and 2) $m_s = 1$ (prepared via π-pulse after initialization) of NVs A and B under our logical green readout sequence, 3)$m_s = 0$ of NV C under our resonant individual readout, and 4) the expected Ramsey signal under the logical green readout, identical to the simultaneous control sequence but with no Rabi oscillations induced on NV C, nor individual readout during the precession interval.

Data analysis

Figure 3-14a shows the raw counts divided by the appropriate normalization counts (G for all measurements on NVs A and B, N for the individual readout on NV C), along with the fits described below. The readout on C is fit with a model for Rabi oscillations with a sinusoidal envelope for the additional hyperfine interaction:

$$\text{Rabi } = [A_1 + A_2 \cos(\omega_1 \tau)] \cos(\omega_2 \tau - \phi) + C_B \tag{3.16}$$

The fit minimum $A_1 + A_2$ is then used to normalize the counts to a population measurement as shown in Figure 3-14b. The raw Ramsey counts (from both reference and simultaneous control M signals) are normalized by the green $m_s = 0$ normalization bin G. These results are plotted in Figure 3-14a. Both Ramsey signals are converted into a population measurement using the following normalization:

$$|c_0|^2 = \frac{M - D}{G - D} \tag{3.17}$$

The reference Ramsey is fit to the following model, with three sinusoids for each of three hyperfine levels, as well as a decay term for the finite NV coherence time T_2:

$$\text{Ramsey } = e^{-\tau/T_2} \Big[A_1 \cos(\omega_1 \tau - \phi_1) + A_2 \cos(\omega_2 \tau - \phi_2) + A_3 \cos(\omega_3 \tau - \phi_3) \Big] + C_M \tag{3.18}$$

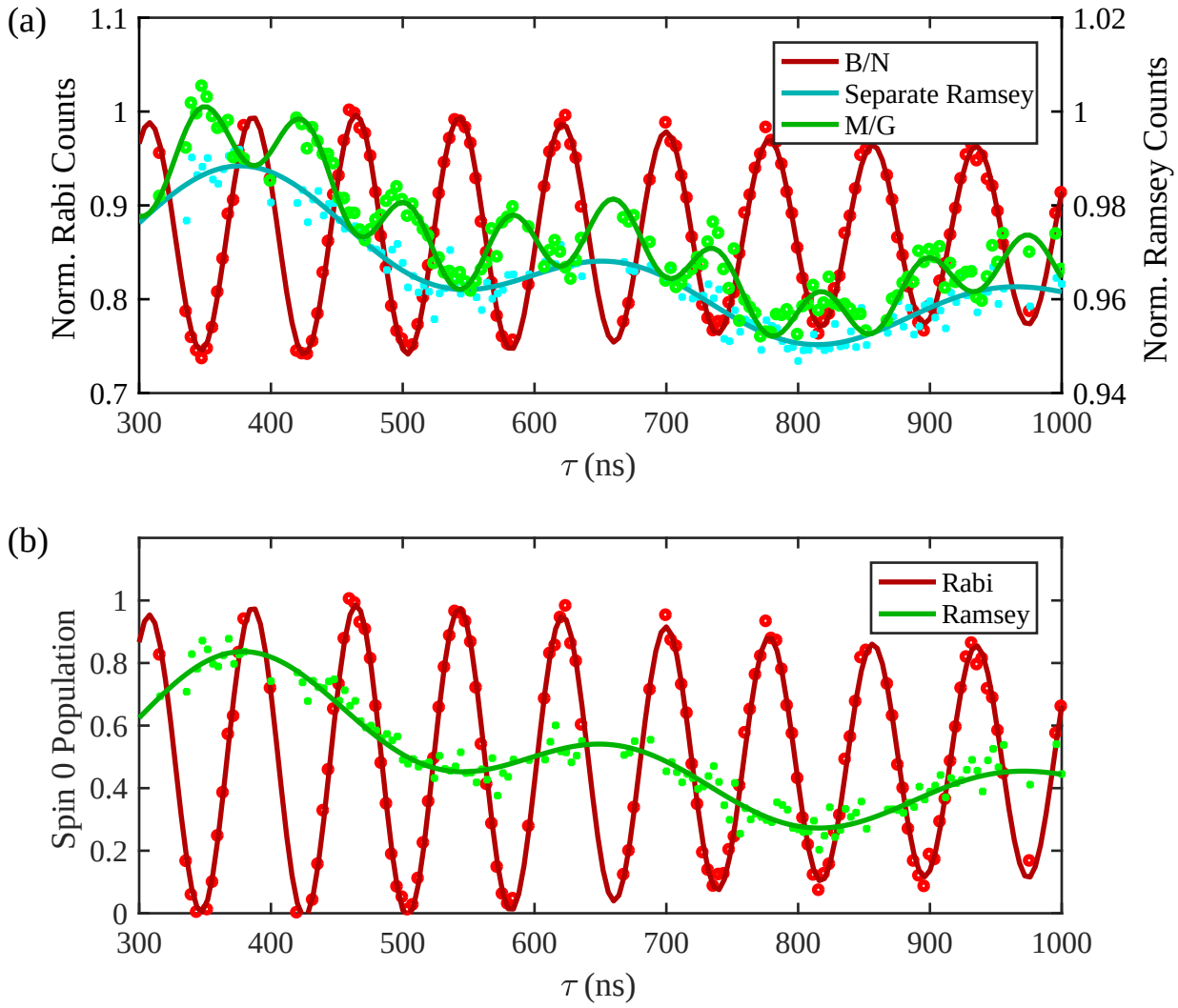

Figure 3-14: (a) Raw normalized data for the individual readout of the Rabi on NV C (red), the reference Ramsey on NVs A and B (blue), and the Ramsey on NVs A and B taken with readout of NV C (green). (b) Final individual control results for both NV systems, normalized and corrected as per the data analysis described in the main text.

For the simultaneous control Ramsey, due to infidelities in the π-pulse during the logical green readout, we see an additional signal from the Rabi on NV C corresponding to imperfect ionization of the $m_s = 1$ state. We thus fit this signal to the following model:

$$A_1 \text{Ramsey} + C_M + A_2(1 - \text{Rabi}) \tag{3.19}$$

Where the "Ramsey" and "Rabi" terms correspond to the fit results of the signal components of the above two models without offsets C_B and C_M, and the C_M term here is similarly not a fit parameter, but the same constant fit in the reference Ramsey. In this way, the only two fit parameters are the fidelity of the Ramsey signal A_1 and the relative contribution from the Rabi signal A_2. Figure 3-14b shows the final Ramsey signal after removing the extraneous Rabi signal, i.e. $A_1\text{Ramsey} + C_M$. The crosstalk fidelity of our readout $\eta = A_1$ is determined to be near unity at $A_1 = 1 \pm 0.04$, indicating that we have no detectable degradation of our signal as a result of the individual readout on NV C. This is consistent with our model; based on the known $\gamma = 13$ MHz, $\Omega = 1.7$ GHz, readout time $T = 300$ ns, and detuning $\Delta = 23$ GHz shown in Figure 3-5b, our model predicts a bit error rate of around 1%, below the 4% fit bounds.

Chapter 4

Conclusion

We have demonstrated that detunings between like resonance transitions in atom-like qubits can be harnessed to enable super-resolution localization and individual readout. In particular, we show sub-nanometer precision localization of NV centers within 100 nm of one another, well below the diffraction limit. More significantly, we perform simultaneous control and readout sequences on multiple NVs, with unity crosstalk fidelity to within experimental precision. This opens the door to a variety of applications, ranging from multi-NV sensing schemes to error-corrected clusters for quantum computing.

4.1 Platform Viability

This thesis utilized a high strain sample specifically chosen to increase the likelihood of finding diffraction-limited clusters with split ZPLs. However, the most promising defect center results have come from using single-crystal, inherently low strain samples [2, 15–19, 41]. One might then reasonably question the applicability of our technique towards future quantum technologies. While we note that applying an electric field gradient can tune NV resonances by some ~ 10 GHz via the Stark Effect [42], which may be sufficient to tune NV centers out of resonance. However, this adds an additional engineering complexity that may be undesirable. To assess the viability of our platform without these active components, we consider the probability of forming systems of multiple, distinguishable emitters in a single crystal, electronic grade diamond implanted with nitrogen (energy 185 eV, dosage 10^9 cm^{-2}).

The classic "Birthday Problem" in statistics considers the probability that a room of N people contains at least two individuals with the same birthday, concluding that $N = 23$ gives a 50.7% probability for at least one overlap. Analogously, we consider the probability that a set of N NVs has no overlapping ZPL transitions — in other words, the probability that each ZPL is at least some detuning Δ away from its nearest neighbor. The Birthday Problem is made easier by assuming a uniform distribution of birthdays across the 365 calendar days; however, the distribution of NV resonances is expected to be more Gaussian in form, making the problem considerably more complex.

Taking advantage of the motorized flip mirrors and rotation mounts in our setup, we perform automated PLE measurements on a 1200 μm^2 field of view of the aforementioned single crystal diamond. Our automatic characterization system identifies 1938 emitter sites based on fluorescence; after taking spectroscopy and performing PLE spectroscopy, 184 of these sites exhibit strong ZPLs with signal-to-noise ratios greater than 3. Specifically, our system finds 373 ZPLs in these 184 sites total, very nearly corresponding to the two expected E_x and E_y transitions per NV. Kernel estimation on this dataset allows construction of an empirical probability distribution for randomly selected NVs in such a diamond. The histogram of the raw data in units of probability density and the associated kernel estimate are shown in Figure 4-1a.

With this empirical distribution, we solve the Birthday Problem via simulation. For each trial, we randomly select N ZPL frequencies from the distribution and determine if they are all at least some desired Δ apart. We repeat this for a range of N and Δ, performing 10^3 trials for each combination. The distribution is not the only empirical component of our simulation; the detunings are specifically chosen based on the expected bit error rate at that detuning as experimentally determined in Section 3.5.2, grounding our results in realistic parameters. Figure 4-1b shows the percentage of trials that exhibited fully distinguishable ZPLs as a function of the number of NVs. From these results, we conclude that registers of 3 NVs per site, our target for a quantum error corrected register, could be created with 15.2% yield and have 99% crosstalk fidelity. These numbers are quite encouraging for near-term generation of such clusters, and their determination based on a single-crystal sample demonstrates the promise of our method for broader quantum information applications.

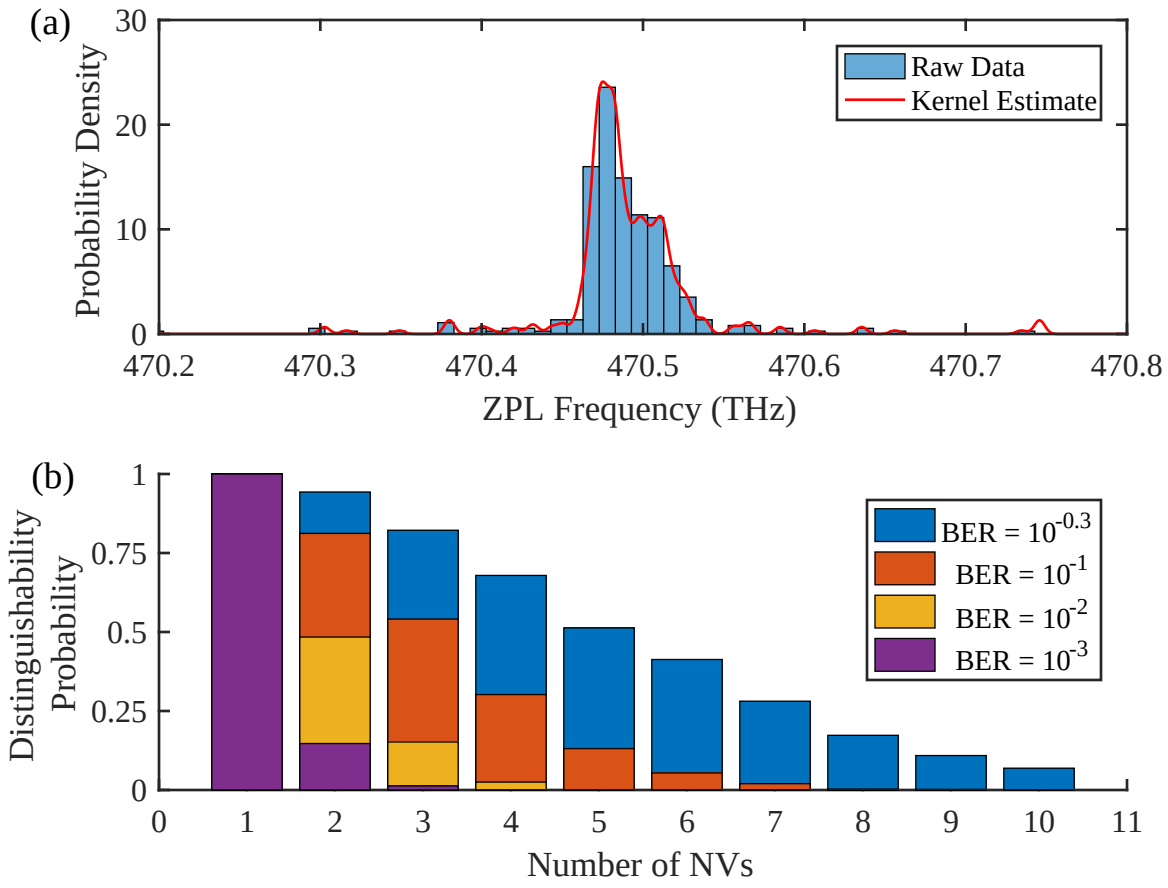

Figure 4-1: (a) Empirical distribution of 373 ZPLs plotted as a histogram normalized to probability density, overlaid by the kernel density estimate used to build our probability density function. (b) Results of the "Birthday Problem" simulation for various register sizes and various maximum tolerances for bit error rate.

4.2 Future Directions

Having demonstrated the proof-of-principle, future efforts will seek to refine this process and more deterministically create registers rather than relying on the probabilistic creation of multi-NV sites. For example, masked nitrogen implantation [43] (Fig. 4-2a) and vacancy generation via focused laser writing [44] or TEM irradiation [45] (Fig. 4-2b) have been used to demonstrate precision creation of NV centers, and could in principle be used to generate localized NV clusters. Thinking more broadly, this technique could be applied to most any solid state qubit system [46]. The inversion-symmetric silicon vacancy (SiV) [47] and germanium vacancy (GeV) [48] centers in diamond have shown promise for quantum infor-

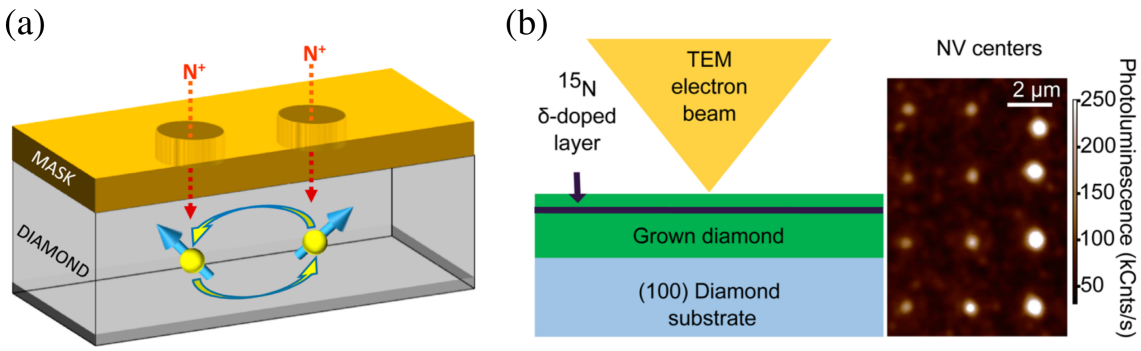

Figure 4-2: (a) Masked implantation has enabled the creation of sub-diffraction NV centers, and could be used to make registers for individual readout. Taken from [43]. (b) Focused TEM irradiation creates localized vacancies, which can form NV centers after high temperature annealing. Taken from [45].

mation applications [41, 49, 50]; while subject to weaker broadening due to their symmetry, they may still prove distinguishable enough to apply our technique. Beyond diamond, defect centers in other materials such as silicon carbide [51], gallium nitride [52], or rare-earth ions in solids [53, 54] could hold promise, as well as artificial atoms like quantum dots [55–57], all of which exhibit appreciable distributions of resonance frequencies.

Bibliography

[1] A. Acín, I. Bloch, H. Buhrman, T. Calarco, C. Eichler, J. Eisert, D. Esteve, N. Gisin, S. J. Glaser, F. Jelezko, S. Kuhr, M. Lewenstein, M. F. Riedel, P. O. Schmidt, R. Thew, A. Wallraff, I. Walmsley, and F. K. Wilhelm. The European Quantum Technologies Roadmap. *arXiv:1712.03773*, December 2017.

[2] B. Hensen, H. Bernien, A. E. Dréau, A. Reiserer, N. Kalb, M. S. Blok, J. Ruitenberg, R. F. L. Vermeulen, R. N. Schouten, C. Abellán, W. Amaya, V. Pruneri, M. W. Mitchell, M. Markham, D. J. Twitchen, D. Elkouss, S. Wehner, T. H. Taminiau, and R. Hanson. Loophole-free bell inequality violation using electron spins separated by 1.3 kilometres. *Nature*, 526:682, 10 2015.

[3] Marissa Giustina, Marijn A. M. Versteegh, Sören Wengerowsky, Johannes Handsteiner, Armin Hochrainer, Kevin Phelan, Fabian Steinlechner, Johannes Kofler, Jan-Åke Larsson, Carlos Abellán, Waldimar Amaya, Valerio Pruneri, Morgan W. Mitchell, Jörn Beyer, Thomas Gerrits, Adriana E. Lita, Lynden K. Shalm, Sae Woo Nam, Thomas Scheidl, Rupert Ursin, Bernhard Wittmann, and Anton Zeilinger. Significant-loophole-free test of bell's theorem with entangled photons. *Phys. Rev. Lett.*, 115:250401, Dec 2015.

[4] Lynden K. Shalm, Evan Meyer-Scott, Bradley G. Christensen, Peter Bierhorst, Michael A. Wayne, Martin J. Stevens, Thomas Gerrits, Scott Glancy, Deny R. Hamel, Michael S. Allman, Kevin J. Coakley, Shellee D. Dyer, Carson Hodge, Adriana E. Lita, Varun B. Verma, Camilla Lambrocco, Edward Tortorici, Alan L. Migdall, Yanbao Zhang, Daniel R. Kumor, William H. Farr, Francesco Marsili, Matthew D. Shaw, Jeffrey A. Stern, Carlos Abellán, Waldimar Amaya, Valerio Pruneri, Thomas Jennewein,

Morgan W. Mitchell, Paul G. Kwiat, Joshua C. Bienfang, Richard P. Mirin, Emanuel Knill, and Sae Woo Nam. Strong loophole-free test of local realism. *Phys. Rev. Lett.*, 115:250402, Dec 2015.

[5] Nissim Ofek, Andrei Petrenko, Reinier Heeres, Philip Reinhold, Zaki Leghtas, Brian Vlastakis, Yehan Liu, Luigi Frunzio, S. M. Girvin, L. Jiang, Mazyar Mirrahimi, M. H. Devoret, and R. J. Schoelkopf. Extending the lifetime of a quantum bit with error correction in superconducting circuits. *Nature*, 536:441, 07 2016.

[6] Jay M. Gambetta, A. D. Córcoles, S. T. Merkel, B. R. Johnson, John A. Smolin, Jerry M. Chow, Colm A. Ryan, Chad Rigetti, S. Poletto, Thomas A. Ohki, Mark B. Ketchen, and M. Steffen. Characterization of addressability by simultaneous randomized benchmarking. *Phys. Rev. Lett.*, 109:240504, Dec 2012.

[7] Jay M. Gambetta, Jerry M. Chow, and Matthias Steffen. Building logical qubits in a superconducting quantum computing system. *npj Quantum Information*, 3(1):2, 2017.

[8] Bjoern Lekitsch, Sebastian Weidt, Austin G. Fowler, Klaus Mølmer, Simon J. Devitt, Christof Wunderlich, and Winfried K. Hensinger. Blueprint for a microwave trapped ion quantum computer. *Science Advances*, 3(2), 2017.

[9] A. Batalov, V. Jacques, F. Kaiser, P. Siyushev, P. Neumann, L. J. Rogers, R. L. McMurtrie, N. B. Manson, F. Jelezko, and J. Wrachtrup. Low temperature studies of the excited-state structure of negatively charged nitrogen-vacancy color centers in diamond. *Phys. Rev. Lett.*, 102:195506, May 2009.

[10] E. Togan, Y. Chu, A. S. Trifonov, L. Jiang, J. Maze, L. Childress, M. V. G. Dutt, A. S. Sørensen, P. R. Hemmer, A. S. Zibrov, and M. D. Lukin. Quantum entanglement between an optical photon and a solid-state spin qubit. *Nature*, 466:730, 08 2010.

[11] M W Doherty, N B Manson, P Delaney, and L C L Hollenberg. The negatively charged nitrogen-vacancy centre in diamond: the electronic solution. *New Journal of Physics*, 13(2):025019, 2011.

[12] M. L. Goldman, A. Sipahigil, M. W. Doherty, N. Y. Yao, S. D. Bennett, M. Markham, D. J. Twitchen, N. B. Manson, A. Kubanek, and M. D. Lukin. Phonon-induced population dynamics and intersystem crossing in nitrogen-vacancy centers. *Phys. Rev. Lett.*, 114:145502, Apr 2015.

[13] Y. Chu and M. D. Lukin. Quantum optics with nitrogen-vacancy centers in diamond. *arXiv:1504.05990*, April 2015.

[14] Marcus W. Doherty, Neil B. Manson, Paul Delaney, Fedor Jelezko, JÃűrg Wrachtrup, and Lloyd C.L. Hollenberg. The nitrogen-vacancy colour centre in diamond. *Physics Reports*, 528(1):1 – 45, 2013. The nitrogen-vacancy colour centre in diamond.

[15] N. Bar-Gill, L. M. Pham, A. Jarmola, D. Budker, and R. L. Walsworth. Solid-state electronic spin coherence time approaching one second. *Nature Communications*, 4:1743, 04 2013.

[16] P. C. Maurer, G. Kucsko, C. Latta, L. Jiang, N. Y. Yao, S. D. Bennett, F. Pastawski, D. Hunger, N. Chisholm, M. Markham, D. J. Twitchen, J. I. Cirac, and M. D. Lukin. Room-temperature quantum bit memory exceeding one second. *Science*, 336(6086):1283–1286, 2012.

[17] W. Pfaff, B. J. Hensen, H. Bernien, S. B. van Dam, M. S. Blok, T. H. Taminiau, M. J. Tiggelman, R. N. Schouten, M. Markham, D. J. Twitchen, and R. Hanson. Unconditional quantum teleportation between distant solid-state quantum bits. *Science*, 345(6196):532–535, 2014.

[18] G. Waldherr, Y. Wang, S. Zaiser, M. Jamali, T. Schulte-Herbruggen, H. Abe, T. Ohshima, J. Isoya, J. F. Du, P. Neumann, and J. Wrachtrup. Quantum error correction in a solid-state hybrid spin register. *Nature*, 506(7487):204–207, 02 2014.

[19] F. Dolde, I. Jakobi, B. Naydenov, N. Zhao, S. Pezzagna, C. Trautmann, J. Meijer, P. Neumann, F. Jelezko, and J. Wrachtrup. Room-temperature entanglement between single defect spins in diamond. *Nature Physics*, 9:139, 02 2013.

[20] Peter W. Shor. Scheme for reducing decoherence in quantum computer memory. *Phys. Rev. A*, 52:R2493–R2496, Oct 1995.

[21] Dave Bacon. Operator quantum error-correcting subsystems for self-correcting quantum memories. *Phys. Rev. A*, 73:012340, Jan 2006.

[22] Mohamed H. Abobeih, Julia Cramer, Michiel A. Bakker, Norbert Kalb, Daniel J. Twitchen, Matthew Markham, and Tim H. Taminiau. One-second coherence for a single electron spin coupled to a multi-qubit nuclear-spin environment. *arXiv:1801.01196*, 2018.

[23] Simon J Devitt, William J Munro, and Kae Nemoto. Quantum error correction for beginners. *Reports on Progress in Physics*, 76(7):076001, 2013.

[24] I. Lovchinsky, A. O. Sushkov, E. Urbach, N. P. de Leon, S. Choi, K. De Greve, R. Evans, R. Gertner, E. Bersin, C. Müller, L. McGuinness, F. Jelezko, R. L. Walsworth, H. Park, and M. D. Lukin. Nuclear magnetic resonance detection and spectroscopy of single proteins using quantum logic. *Science*, 351(6275):836–841, 2016.

[25] Vittorio Giovannetti, Seth Lloyd, and Lorenzo Maccone. Advances in quantum metrology. *Nature Photonics*, 5:222, 03 2011.

[26] Tohru Tanaka, Paul Knott, Yuichiro Matsuzaki, Shane Dooley, Hiroshi Yamaguchi, William J. Munro, and Shiro Saito. Proposed robust entanglement-based magnetic field sensor beyond the standard quantum limit. *Phys. Rev. Lett.*, 115:170801, Oct 2015.

[27] Jean-Christophe Jaskula, Erik Bauch, Silvia Arroyo-Camejo, Mikhail D. Lukin, Stefan W. Hell, Alexei S. Trifonov, and Ronald L. Walsworth. Superresolution optical magnetic imaging and spectroscopy using individual electronic spins in diamond. *Opt. Express*, 25(10):11048–11064, May 2017.

[28] P. C. Maurer, J. R. Maze, P. L. Stanwix, L. Jiang, A. V. Gorshkov, A. A. Zibrov, B. Harke, J. S. Hodges, A. S. Zibrov, A. Yacoby, D. Twitchen, S. W. Hell, R. L. Walsworth, and M. D. Lukin. Far-field optical imaging and manipulation of individual spins with nanoscale resolution. *Nature Physics*, 6:912, 09 2010.

[29] Shen Li, Xiang dong Chen, Bo-Wen Zhao, Yang Dong, Chong-Wen Zou, Guang-Can Guo, and Fang-Wen Sun. Optical far-field super-resolution microscopy using nitrogen vacancy center ensemble in bulk diamond. *Applied Physics Letters*, 109(11):111107, 2016.

[30] N Aslam, G Waldherr, P Neumann, F Jelezko, and J Wrachtrup. Photo-induced ionization dynamics of the nitrogen vacancy defect in diamond investigated by single-shot charge state detection. *New Journal of Physics*, 15(1):013064, 2013.

[31] P. Siyushev, H. Pinto, M. Vörös, A. Gali, F. Jelezko, and J. Wrachtrup. Optically controlled switching of the charge state of a single nitrogen-vacancy center in diamond at cryogenic temperatures. *Phys. Rev. Lett.*, 110:167402, Apr 2013.

[32] Edward H. Chen, Ophir Gaathon, Matthew E. Trusheim, and Dirk Englund. Wide-field multispectral super-resolution imaging using spin-dependent fluorescence in nanodiamonds. *Nano Letters*, 13(5):2073–2077, 2013. PMID: 23547791.

[33] J R Maze, A Gali, E Togan, Y Chu, A Trifonov, E Kaxiras, and M D Lukin. Properties of nitrogen-vacancy centers in diamond: the group theoretic approach. *New Journal of Physics*, 13(2):025025, 2011.

[34] Matthew E Trusheim and Dirk Englund. Wide-field strain imaging with preferentially aligned nitrogen-vacancy centers in polycrystalline diamond. *New Journal of Physics*, 18(12):123023, 2016.

[35] G. Davies and M. F. Hamer. Optical studies of the 1.945 ev vibronic band in diamond. *Proceedings of the Royal Society of London A: Mathematical, Physical and Engineering Sciences*, 348(1653):285–298, 1976.

[36] D. Howell, I. G. Wood, D. P. Dobson, A. P. Jones, L. Nasdala, and J. W. Harris. Quantifying strain birefringence halos around inclusions in diamond. *Contributions to Mineralogy and Petrology*, 160(5):705–717, Nov 2010.

[37] H. Bernien, B. Hensen, W. Pfaff, G. Koolstra, M. S. Blok, L. Robledo, T. H. Taminiau, M. Markham, D. J. Twitchen, L. Childress, and R. Hanson. Heralded entanglement between solid-state qubits separated by three metres. *Nature*, 497:86, 04 2013.

[38] Y. Chu, N.P. de Leon, B.J. Shields, B. Hausmann, R. Evans, E. Togan, M. J. Burek, M. Markham, A. Stacey, A.S. Zibrov, A. Yacoby, D.J. Twitchen, M. Loncar, H. Park, P. Maletinsky, and M.D. Lukin. Coherent optical transitions in implanted nitrogen vacancy centers. *Nano Letters*, 14(4):1982–1986, 2014. PMID: 24588353.

[39] Janik Wolters, Nikola Sadzak, Andreas W. Schell, Tim Schröder, and Oliver Benson. Measurement of the ultrafast spectral diffusion of the optical transition of nitrogen vacancy centers in nano-size diamond using correlation interferometry. *Phys. Rev. Lett.*, 110:027401, Jan 2013.

[40] Roy J. Glauber. The quantum theory of optical coherence. *Phys. Rev.*, 130:2529–2539, Jun 1963.

[41] A. Sipahigil, R. E. Evans, D. D. Sukachev, M. J. Burek, J. Borregaard, M. K. Bhaskar, C. T. Nguyen, J. L. Pacheco, H. A. Atikian, C. Meuwly, R. M. Camacho, F. Jelezko, E. Bielejec, H. Park, M. Lon**c**ar, and M. D. Lukin. An integrated diamond nanophotonics platform for quantum-optical networks. *Science*, 354(6314):847–850, 2016.

[42] L. C. Bassett, F. J. Heremans, C. G. Yale, B. B. Buckley, and D. D. Awschalom. Electrical tuning of single nitrogen-vacancy center optical transitions enhanced by photoinduced fields. *Phys. Rev. Lett.*, 107:266403, Dec 2011.

[43] Diego Scarabelli, Matt Trusheim, Ophir Gaathon, Dirk Englund, and Shalom J. Wind. Nanoscale engineering of closely-spaced electronic spins in diamond. *Nano Letters*, 16(8):4982–4990, 2016. PMID: 27428077.

[44] Yu-Chen Chen, Patrick S. Salter, Sebastian Knauer, Laiyi Weng, Angelo C. Frangeskou, Colin J. Stephen, Shazeaa N. Ishmael, Philip R. Dolan, Sam Johnson, Ben L. Green, Gavin W. Morley, Mark E. Newton, John G. Rarity, Martin J. Booth, and Jason M.

Smith. Laser writing of coherent colour centres in diamond. *Nature Photonics*, 11:77, 12 2016.

[45] Claire A. McLellan, Bryan A. Myers, Stephan Kraemer, Kenichi Ohno, David D. Awschalom, and Ania C. Bleszynski Jayich. Patterned formation of highly coherent nitrogen-vacancy centers using a focused electron irradiation technique. *Nano Letters*, 16(4):2450–2454, 2016. PMID: 27010642.

[46] Igor Aharonovich, Dirk Englund, and Milos Toth. Solid-state single-photon emitters. *Nature Photonics*, 10:631, 09 2016.

[47] A. Sipahigil, K. D. Jahnke, L. J. Rogers, T. Teraji, J. Isoya, A. S. Zibrov, F. Jelezko, and M. D. Lukin. Indistinguishable photons from separated silicon-vacancy centers in diamond. *Phys. Rev. Lett.*, 113:113602, Sep 2014.

[48] Takayuki Iwasaki, Fumitaka Ishibashi, Yoshiyuki Miyamoto, Yuki Doi, Satoshi Kobayashi, Takehide Miyazaki, Kosuke Tahara, Kay D. Jahnke, Lachlan J. Rogers, Boris Naydenov, Fedor Jelezko, Satoshi Yamasaki, Shinji Nagamachi, Toshiro Inubushi, Norikazu Mizuochi, and Mutsuko Hatano. Germanium-vacancy single color centers in diamond. *Scientific Reports*, 5:12882, 08 2015.

[49] D. D. Sukachev, A. Sipahigil, C. T. Nguyen, M. K. Bhaskar, R. E. Evans, F. Jelezko, and M. D. Lukin. Silicon-vacancy spin qubit in diamond: A quantum memory exceeding 10 ms with single-shot state readout. *Phys. Rev. Lett.*, 119:223602, Nov 2017.

[50] M. K. Bhaskar, D. D. Sukachev, A. Sipahigil, R. E. Evans, M. J. Burek, C. T. Nguyen, L. J. Rogers, P. Siyushev, M. H. Metsch, H. Park, F. Jelezko, M. Lon**c**ar, and M. D. Lukin. Quantum nonlinear optics with a germanium-vacancy color center in a nanoscale diamond waveguide. *Phys. Rev. Lett.*, 118:223603, May 2017.

[51] David J. Christle, Abram L. Falk, Paolo Andrich, Paul V. Klimov, Jawad Ul Hassan, Nguyen T. Son, Erik Janzén, Takeshi Ohshima, and David D. Awschalom. Isolated electron spins in silicon carbide with millisecond coherence times. *Nature Materials*, 14:160, 12 2014.

[52] Amanuel M. Berhane, Kwang-Yong Jeong, ZoltÃąn Bodrog, Saskia Fiedler, Tim SchrÃűder, Noelia Vico TriviÃśo, TomÃąs Palacios, Adam Gali, Milos Toth, Dirk Englund, and Igor Aharonovich. Bright room-temperature single-photon emission from defects in gallium nitride. *Advanced Materials*, 29(12):1605092, 2017. 1605092.

[53] Hugues de Riedmatten, Mikael Afzelius, Matthias U. Staudt, Christoph Simon, and Nicolas Gisin. A solid-state light–matter interface at the single-photon level. *Nature*, 456:773, 12 2008.

[54] Alan Dibos, Mouktik Raha, Chris Phenicie, and Jeff Thompson. Isolating and enhancing the emission of single erbium ions using a silicon nanophotonic cavity. *arXiv:1711.10368*, 2017.

[55] M. H. Baier, S. Watanabe, E. Pelucchi, and E. Kapon. High uniformity of site-controlled pyramidal quantum dots grown on prepatterned substrates. *Applied Physics Letters*, 84(11):1943–1945, 2004.

[56] Arun Mohan, Pascal Gallo, Marco Felici, Benjamin Dwir, Alok Rudra, Jerome Faist, and Eli Kapon. Record-low inhomogeneous broadening of site-controlled quantum dots for nanophotonics. *Small*, 6(12):1268–1272, 2010.

[57] Pascale Senellart, Glenn Solomon, and Andrew White. High-performance semiconductor quantum-dot single-photon sources. *Nature Nanotechnology*, 12:1026, 11 2017.